Journal of Industrial and Engineering Chemistry 112 (2022) 106–124

Contents lists available at ScienceDirect

Journal of Industrial and Engineering Chemistry

journal homepage: www.elsevier.com/locate/jiec

Physical structure, TD-DFT computations, and optical properties of hybrid nanocomposite thin film as optoelectronic devices

M. Sh. Zoromba [a,b,*], H.A. Maddah [a], M.H. Abdel-Aziz [a,c,*], Ahmed F. Al-Hossainy [d]

[a] Chemical and Materials Engineering Department, King Abdulaziz University, Rabigh 21911, Saudi Arabia
[b] Chemistry Department, Faculty of Science, 23 December Street, 42521, Port-Said University, Port-Said, Egypt
[c] Chemical Engineering Department, Faculty of Engineering, Alexandria University, Alexandria, Egypt
[d] Chemistry Department, Faculty of Science, New Valley University, 72511 Al-Wadi Al-Gadid, Al-Kharga, Egypt

ARTICLE INFO

Article history:
Received 4 March 2022
Revised 20 April 2022
Accepted 2 May 2022
Available online 7 May 2022

Keywords:
Hybrid nanocomposite
ZrO_2 nanoparticles
Bandgap
$[P(o\text{-}PDM+m\text{-}PDM)/ZrO_2]^{NC}$
Optical properties

ABSTRACT

HCl doped-copolymer of ortho phenylene diamine and meta phenylene diamine was prepared by using oxidative polymerization method with ferric chloride as an oxidizing agent in the existence of sodium dedocyl sulphate as a soft template. The microporous structure thin films of hybrid copolymer/ZrO_2 nanocomposite $[copolymer/ZrO_2]^{NC}$ were fabricated using a physical vapor deposition (PVD) method. The effect of addition of zirconium oxide nanoparticles $[ZrO_2]^{NPs}$ on the physical properties of the copolymer was discussed in the light of crystallinity and optical properties. The average crystallite size of $[ZrO_2]^{NPs}$ is around 40 nm. The copolymer showed an absorbance of 1.18 at the wavelength (λ) 374 nm, which increased to 1.26 at λ = 440 nm after glycine addition, also increased to 1.53 at λ = 486 nm after $[ZrO_2]^{NPs}$ loading. Also, the significant changes in the absorption index and indirect/direct bandgap of the copolymer have been detected. The *materials Studio 7.0 program* on TDDFT/DMol^3 was used to optimize the molecular structure and perform the frequency calculations for the crystal models and isolated molecules. The DFT-Gaussian09W-vibration values are quite similar to the experimental data either in the structure or in the optical properties. The improvements in optical properties were achieved and revealed the possibility of using the hybrid nanocomposite films in the polymers solar cell application.

Introduction

Metal oxide semiconductors have gotten a lot of consideration as potential thin film transistor channel materials (TFTs). Because the charge accumulated determines the field-induced current, utilizing a high dielectric constant material as the gate dielectric, which allows for a larger surface charge density at the semiconductor/dielectric interface, is a suitable strategy for attaining low-voltage operation in TFT. To get around this hurdle, researchers have looked into a variety of methods for making huge areal-capacitance gate insulators [1–4]. Zirconium oxide (ZrO_2) is a fascinating semiconducting material with a broad bandgap that has been extensively studied in attempt to understand its fundamental properties in order to fabricate highly efficient devices [5–7]. As the processing temperature rises, the bandgap of ZrO_2 reduces, making it more accommodating and thus suited for application-oriented research. ZrO_2 is characterized by a high melting point, high mechanical and thermal resistance, a high dielectric constant, and low electrical conductivity. ZrO_2 is a great choice for chemical, optical, dielectric, and mechanical applications because of its chemical stability, high hardness, and biocompatibility [8–11]. ZrO_2 could be useful in fuel cells [12], mirror protection coatings, and optoelectronic devices [13]. Building-integrated photovoltaics (BIPV) technology has advanced significantly in the previous decade [14,15].

On the other hand, aromatic diamine conjugated polymers are remarkable in that they have a wide range of properties, including good electroactivity, flexible conductivity, attractive electrochromic, and magnetic activity [16–18]. These properties are unique due to their multifunctional architectures, which include linear polyaminonaphthylamine, linear polyaminoaniline, and polyphenazine or phenazine ladder units inside the polymer chains. Polyphenylene diamines have thus been produced and investigated for applications in electrocatalysis, electrochromic, sensors, and electrode materials [19–22]. Due to the presence of π -conjugated structure in conjugated polymers, these polymers can be included in the characteristics of other

* Corresponding authors.
E-mail addresses: mzoromba@kau.edu.sa (M. Sh. Zoromba), mhmossa@kau.edu.sa (M.H. Abdel-Aziz).

https://doi.org/10.1016/j.jiec.2022.05.004
1226-086X/

polymers. The conjugated polymers have an alternate molecular structure of single and double bonds throughout their chain, which allows them to conduct depending on π bond delocalization. The band-gap energy is reduced as a result of electron delocalization, and the molecule's ground state energy is reduced as a result. Conjugated polymers can be used in a wide range of applications. Various electronic devices made of conducting polymers have recently been developed as an alternative for inorganic semiconducting materials [23,24]. With different polymerization methods, media, and conditions, the chemical structures, molecular weights, and physical properties of the produced polyphenylene diamines vary greatly. The creation of aromatic diamine polymers through oxidation of one or both amino groups to generate a structure with an open ring with substitution functional groups or a ladder structure is the most recent advancement in this area [25]. The optoelectronic properties of polyphenylene diamines, which are conducting polymers, have piqued researchers' curiosity. Inorganic semiconductor complexes, such as polyphenylene diamines, have also been the focus of much research in nanoscience and nanotechnology for applications such as light-emitting transistors, polymer light-emitting transistors, and polymer solar cells [26–28]. As original carbon-based functional class polymers, polyphenylene diamines improve a variety of qualities, including electrical and mechanical capabilities. Because of the stretch-conjugation with the polymeric backbone, they have a high conductivity [29]. ZrO_2-(aniline (AN) and p-nitroaniline (PNAn) copolymer hybrid nanocomposite thin film with energy bandgaps of 2.307 eV and 1.711 eV was fabricated and the solar cell's photovoltaic activity was explored. At light intensities of 60 and 240 mW/cm^2, the power conversion efficiency ranged from 4.275 to 7.125 % [30].

In this work, the novel hybrid polymer nanocomposites of HCl doped-copolymer of ortho phenylene diamine and meta phenylene diamine/ZrO_2 were prepared by PVD technique and characterized using (XRD), (FTIR), and (SEM). HR-TEM and XRD were used to investigate the shape and size of nanocomposites. These films are investigated in terms of their optical, and electrical characteristics. The aim is to improve band gap tenability, and optical properties to expand the uses of hybrid nanocomposite in the semiconductor sector.

Experimental tools and measurements

Raw materials

Except for ortho and meta phenylenediamine, all chemical ingredients were used as obtained, with no further treatment. Before usage, aniline was subjected to two distillations and stored in a dark bottle. Aldrich provided meta phenylenediamine, ortho phenylenediamine, sodium dodecyl sulphate, and hydrochloric

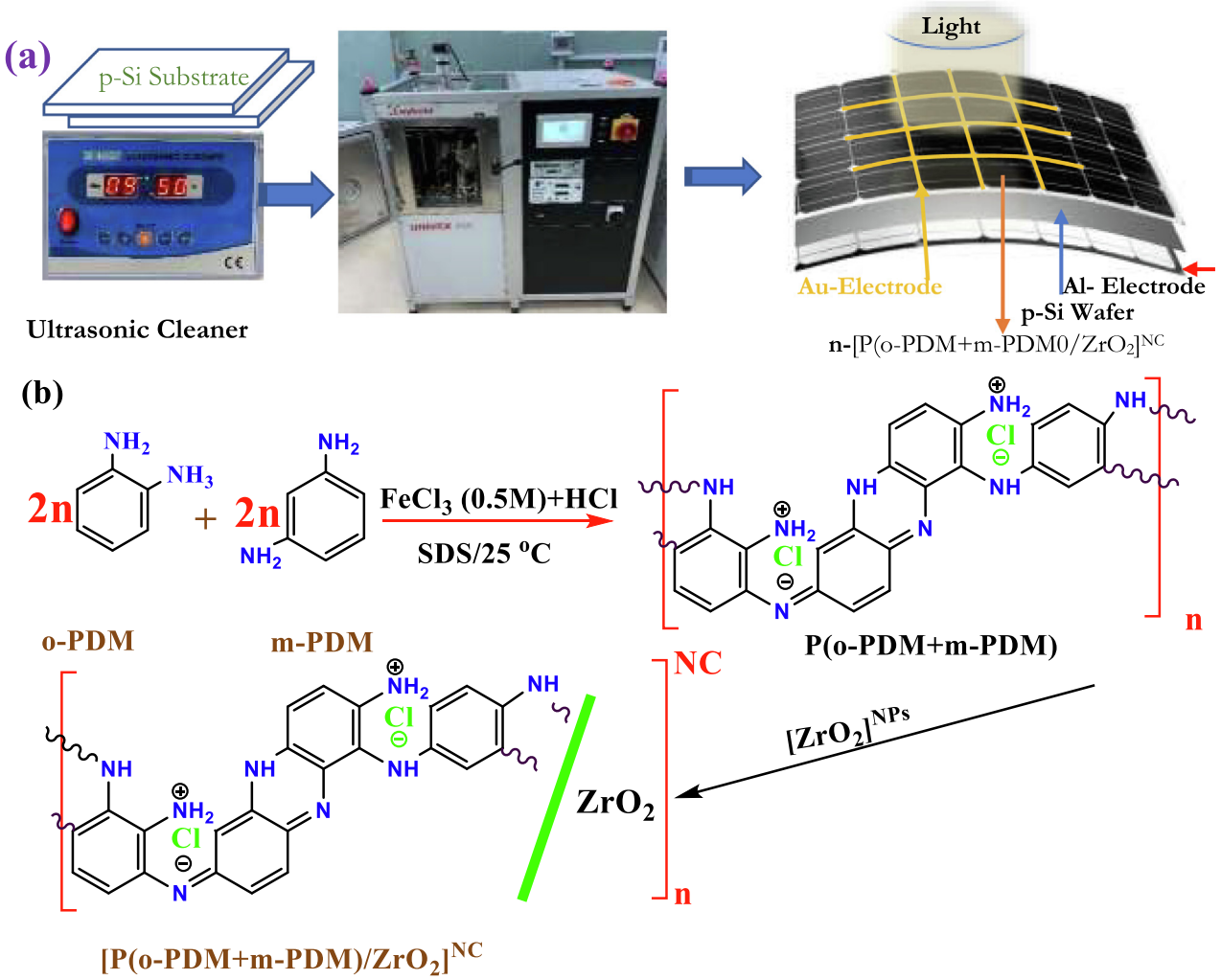

Fig. 1. a) Fabrication of hybrid polymer solar cell Au/n-[P(o-PDM + m-PDM)/ZrO_2]^{NC}/p-Si/Al. b) Suggested scheme of synthesis [P(o-PDM + m-PDM)/ZrO_2]^{NC}.

Table 1
List of analyses methods and equipment.

Analytical methods	Types and models
FT-IR	Perkin-Elmer FT-IR type 1650 spectrophotometer.
Raman spectra	Nicolet iS50 FT-IR (Thermos Scientific) system equipped with a He–Ne laser emitting monochromatic red light at a power of 28 mW.
XRD	A RIGAKUU Ultimo IV XRD / Cu Kα radiation (λ = 1.5418 Å)
Optical measurements photoluminescence	Shimadzu UV-3600 UV–vis NIR spectrophotometer. Hitachi F-7100 fluorescence spectrometer equipped with a detector photomultiplier R928F.

acid. Ferric chloride (anhydrous), dimethyl sulfoxide (DMSO), and analytical grade ethanol were given by Shanghai chemicals. Merch provided zinc acetate dihydride salts ($Zn(CH_3COO)_2.2H_2O$) and polyethylene glycol (PEG)-6000. SD Fine Chemicals Ltd. (Mumbai, India) provided acetic acid with chemical pure quality. These compounds were utilized without additional purification as received.

Synthesis of the copolymer

Under magnetic stirrer, 2.16 g ortho phenylene diamine and 2.16 g meta phenylene diamine were dissolved in 60 mL ethanol. To the prior co-monomer's solution, 5 mL (32% HCl) was added. 2.88 grams of sodium dodecyl sulphate surfactant were dissolved in 150 milliliters of distilled water separately. In the co-monomer's solution, the surfactant solution was added. Drop by drop, 160 mL FeCl3(0.5 M) solution was added to the co-monomer's solution for 2 hours at room temperature using a magnetic stirrer at 900 rpm. The resultant copolymer was left overnight before being filtered and rinsed with distilled water numerous times. The polymer was dried in a 70 °C oven.

Synthesis of the copolymer/ZrO_2 nanocomposite

Using a magnetic stirrer, the needed volumes of the copolymer were dissolved individually in 50 mL of dimethyl sulfoxide (DMSO) for 1 hour at 80 °C until the copolymer was completely dissolved. The hybrid polymer nanocomposites films (HPNCs) were synthesized by mixing of the copolymer with $[ZrO_2]^{NPs}$ fabricated utilizing sol–gel. This was performed using the equation [31]:

$$x(wt.\%) = (W_{ZrO_2}/W_b + W_{ZrO_2}) \times 100 \quad (1)$$

where W_{ZrO_2} and W_b are the weights of nanoparticles and copolymer, correspondingly, with the $[ZrO_2]^{NPs}$ concentrations set at 2.5, 5.0, and 7.5% [32]. The HPNCs solutions were mixed at room temperature for two hours to ensure homogeneous dispersion over the NPs, then cast in Petri plates and dried for 20 hours at 40 °C. The fabricated thin films (with thickness 100 ± 3 nm) were deposited onto a p-Si wafer and ITO/glass substrate utilizing physical vapor deposition (PVD technique) by using a UNIVEX 250 Leybold (Germany). The thickness of film was computed by M − 2000 Ellipsometer and found 100 ± 3 nm. From Fig. 1, the nano-spherical $[P(o\text{-PDM} + m\text{-PDM})/ZrO_2]^{NC}$ derivatives thin films were fabricated under at fix vacuum pressure [33]. The technique of PVD was used to manufacture thin films of $[P(o\text{-PDM} + m\text{-PDM0}/ZrO_2]^{NC}$ derivatives on a p-Si wafer substrate (10 × 5 mm with 0.2 m thickness; Front side), followed by deposition of the thin film on pure Au (60 nm). The Al- electrode was produced with a thickness of 95 nm on the backside of the p-Si wafer substrate utilizing magnetron sputtering. The hybrid polymer solar cell Au/n-$[P(o\text{-PDM} + m\text{-PDM})/ZrO_2]^{NC}$ /p-Si/Al was produced with a photoactive region of 6.25 × 10^5 m^2 [34].

Computational study of $P(o\text{-PDM} + m\text{-PDM})/ZrO_2]^{NC}$ as an isolated molecule in the cell unit

The Materials Studio 7.0 program on TDDFT/$DMol^3$ was used to optimize the molecular structure and perform the frequency calculations for the crystal models and isolated molecules. The norm-conserving pseudopotential generalized gradient approximation at Perdew–Burke–Ernzerh of correlation functional, and the double numerical plus polarization (DNP) basis set were completed for isolated molecules in the gaseous state using TDDFT/$DMol^3$ method [35]. The value of plane-wave cut-off energy was 830 eV, and geometry properties were computed at the gamma point from $DMol^3$ frequency calculations with the GAUSSIAN 09 W software program. After the task type was selected as optimization + fre quency, the ground state option was employed, and then the TDDFT default and the WBX97XD/6–311 G spin and basis set were selected [36].

Characterization

Table 1 shows the instruments used to characterize the solution and powder samples, as well as the fabricated $[P(o\text{-PDM} + m\text{-PDM})]^{TF}$ and $[P(o\text{-PDM} + m\text{-PDM})/ZrO_2]^{NC}$.

Results and discussions

FTIR of P(o-PDM + m-PDM) and $[P(o\text{-PDM} + m\text{-PDM})/ZrO_2]^{NC}$ thin films

Chemical changes in the polymer's structure can be detected using FTIR spectroscopy (Vertex 80v powder FT-IR spectrometer (Bruker Optics, Germany). The experiment was carried out at room temperature in the region of 450–4000 cm^{-1}. The experimental and computed IR spectrum of pristine copolymer and the composite, respectively, are shown in Fig. 2. The distinct bands shown at 1396, 3215, 890, and 766 cm^{-1} can be attributed to the hydroxide group of the water molecule, which is associated to bending, stretching, rocking, and wagging vibrations, as illustrated in the spectrum. This shows that water molecules are present in the copolymer [37,38]. Out of plane-bending vibrations (C–H) in benzene backbones are responsible for the sharp bands that appeared at 766 and 890 cm^{-1}. Sharp band located at 3365 cm^{-1} for the neat copolymer, this can be due to the existence of $–NH_2$ group pending through backbones of the copolymer. The neat copolymer has a sharp band at 3365 cm^{-1}, which could be attributed to the presence of the $–NH_2$ group pending through the backbones of the copolymer. The –NH stretching, vibration characteristic band occurred at 3215 and 3288 cm^{-1} for neat copolymer and its composite, respectively. This shift in wavenumber takes place for –NH ($\cong$73 $cm^{-1)}$ can be attributed to the interaction between unoccupied molecular orbitals (UMO) of ZrO_2 nanoparticle and occupied molecular orbitals (OMO) copolymer to formation nanocomposite. The bands at 1625 cm^{-1} and 1516 cm^{-1} are indicative of quinonoid and benzenoid stretching vibrations for neat copolymer, while in the composite case the characteristics bands for quinonoid and benzenoid structure were shifted 1666 cm^{-1} and 1553 cm^{-1}. Shifts were found to be + 41 cm^{-1} and + 37 cm^{-1} for quinonoid and benzenoid forms respectively. These shifts can be attributed to formation of physical bonds between zirconium oxide and copolymer via quinonoid structure. The physical interaction of ZrO_2 with the copolymer forming the composite is responsible for this shift. On the other hand, in the composite, new bands developed in additional bands at 454 and 494 cm^{-1}. While these bands did not show in the pristine copolymer, they are designed to (O = Zr = O) [39,40].

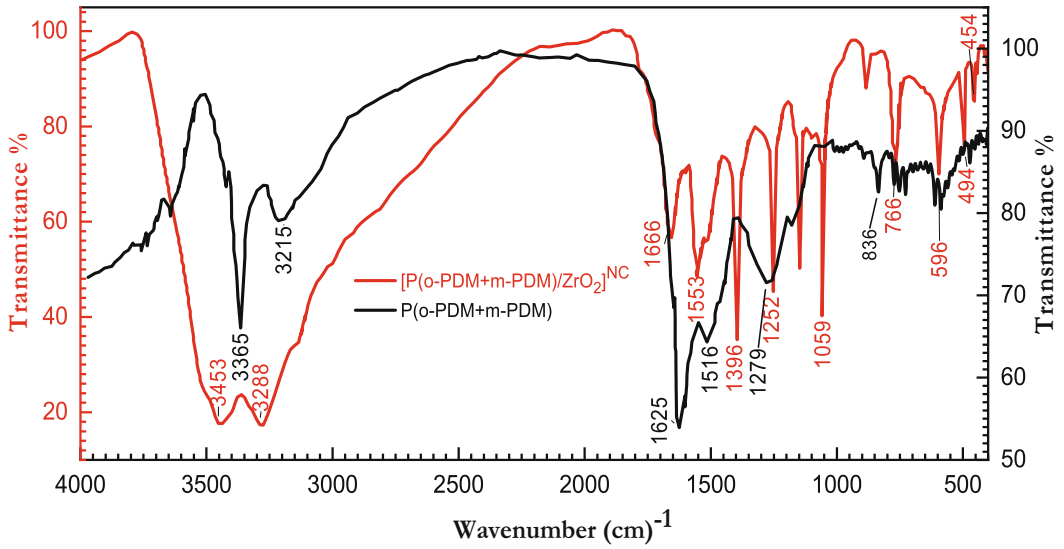

Fig. 2. FTIR of the P(o-PDM + m-PDM) and [P(o-PDM + m-PDM)/ZrO_2]^{NC} thin films.

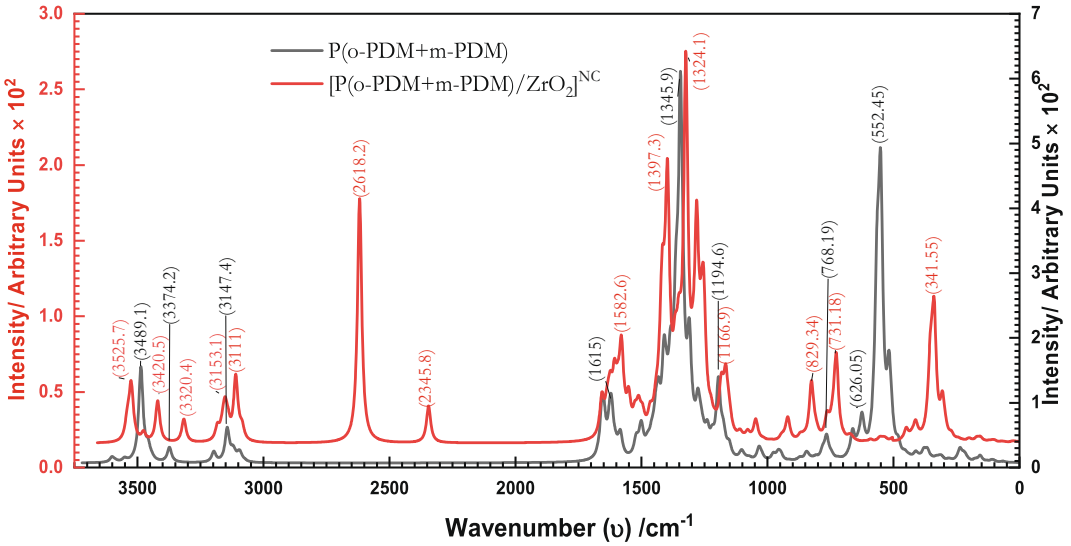

Fig. 3. Raman spectra of the P(o-PDM + m-PDM) and [P(o-PDM + m-PDM)/ZrO_2]$^{NC.}$

Raman spectra of P(o-PDM + m-PDM) and [P(o-PDM + m-PDM)/ZrO_2]^{NC}

The Raman spectrum of the copolymer and composite depicted in Fig. 3 contains four major bands at approximately ($3000 \leq \upsilon \leq 3600$), ($2300 \leq \upsilon \leq 2650$), ($1000 \leq \upsilon \leq 1650$), and ($300 \leq \upsilon \leq 900$) cm^{-1}, which correspond to the NH_2 group stretching, appear only in composite due to (ZrO_2-NH) stretching, double bond in quinonoid and benzenoid structure stretching, and double bond of metal (Zr) and Oxide bending modes, respectively [41]. In comparison, the nanocomposite seen in Fig. 3 displays a strong, strongly defined Raman spectra with distinct bands, which is typical of crystalline nanocomposite material. A study was conducted to assess the precision with which the individual Raman band locations could be calculated. The results are shown in Fig. 3, where it can be observed that measurements obtained at the same position have very little dispersion, while appear new peak only in two positions at range 2618 cm^{-1} and 341 cm^{-1} in nanocomposite. This peak can attributed to the stretching of linked [ZrO_2]^{NPs} with copolymer at –NH groups and double bond of Zr = O starching, respectively.

Thermal analysis of the samples

In Fig. 4 (TGA, DrTGA and DTA), the thermogravimetric curves of PoPDApT show many peaks with different temperatures 25 °C ≤ T ≤ 800 °C for the heating rate of 10 °C/min under nitrogen atmosphere. From thermogravimetric data (TGA, DrTGA and DTA), it can be noted that decomposition of the copolymer and the composite appears in three main thermal stages. The first stage took place in the range of 30–225 °C. While the mass loss 15.98% can be attributed to the removal of (moisture, lattice, and coordinate) water and HCl molecules which result from the decomposition of the dopant emeraldine copolymer salt [15], the presence of water

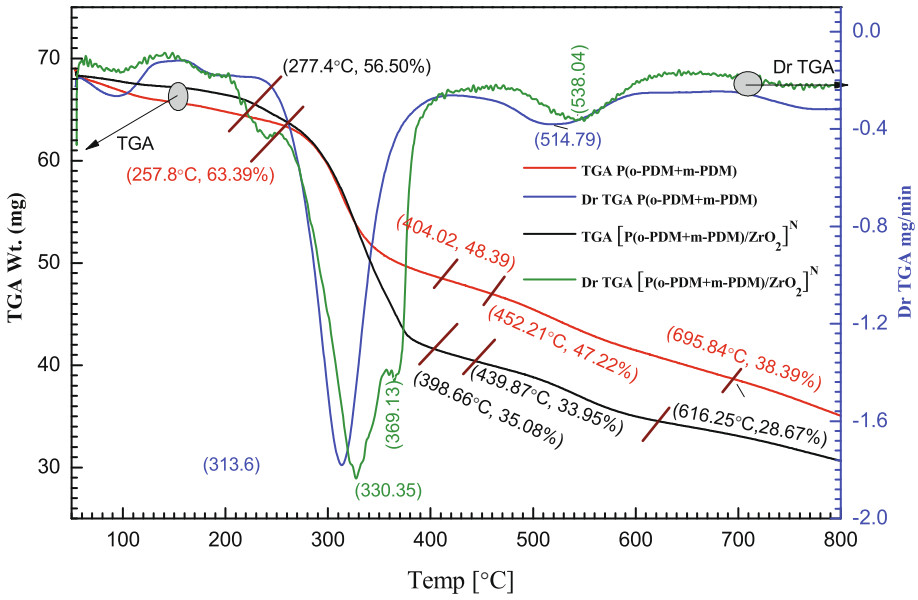

Fig. 4. Thermogravimetric analysis of the copolymer and composite.

molecules was confirmed by FTIR analysis. The second stage occurred in the range of 225 – 402 °C (DTG peak at 330 °C and 313 for copolymer and the composite respectively). The mass loss 20% corresponds to the thermo-oxidative decomposition of the copolymer chains either in the copolymer or in the composite. The third stage came about in the range of 403 – 690 °C (DTG peak at 515 °C and 330 °C for the copolymer and composite respectively); the decomposition of the remaining benzene rings occurred in the third stage at mass loss 10% and 9% for the copolymer and the composite, respectively.

The shoulder peak at 369 °C in the range 355 – 414 °C corresponded to a weight loss of the remaining quinonoid ring in composite matrix. This result indicated that the shoulder peak could be attributed to the decomposition of quinonoid nanocomposite groups. As shown in Fig. 4, the DTG curve has two well-separated peaks in both copolymer and composite due to the decomposition of the copolymer moieties that took place in the second and third stages, respectively. Such observation indicates that the decomposition was carried out through two steps with DTA peaks.

Sem

In Fig. 5a, the flakes of individual copolymer [P(o-PDM + m-PDM)] is seen in the SEM image. The evidence of the enhanced dispersion of $[ZrO_2]^{NPs}$ in the $[P(o\text{-PDM + m-PDM})/ZrO_2]^{NC}$ nanocomposite matrix can be seen in the SEM images of Fig. 5 b, c and d. The spherical shapes of zirconium oxide nanoparticles $[ZrO_2]^{NPs}$ are easily identified. $[ZrO_2]^{NPs}$ are imbedded in the copolymers and it is easy to discern one from the other.

Hrtem

Fig. 6 shows HRTEM image of the composite thin film at two different magnifications. As shown from the image, the copolymer displayed ZrO_2 embedded in the copolymer forming matrix or the copolymer is surrounding of ZrO_2. The image displayed a sphere-shaped particle with less than 100 nm. Fig. 5 shows some agglomeration between the ZrO_2 in the composite thin film. This agglomeration can be due to the high surface area of the ZrO_2 nanoparticles.

XRD analysis

The combined XRD patterns of $[P(o\text{-PDM + m-PDM})]^{TF}$ and $[P(o\text{-PDM + m-PDM})/ZrO_2]^{NC}$ as experimental part and $[P(o\text{-PDM + m-PDM})]$ and $[P(o\text{-PDM + m-PDM})/ZrO_2]$ as an isolated molecule (Simulated part by using TD-DFT method) are displayed in Fig. 7 (a, b). The intermolecular interference between copolymer thin film and nanocomposite chains may account for the strong peaks at miller indices (hkl) at (110), $(\bar{3}\ 01)$ and (031) for copolymer is shows in Fig. 7a. According to Ortéga et al. [42], the intermolecular interference between copolymer chains may account for the strong peaks at 110), $(\bar{3}\ 01)$ and (031). Reflection of the *Orthorhombic* symmetry in the space group corresponds to *Pbca(61)*. According to database code amcsd 0016694, this corresponds to the actual value of 2θ, d-spacing and miller index (*hkl*) [43]. Another minor peak appears at (*hkl*) equals to (010), (001), $(1\bar{3}0)$, (012), $(2\bar{1}1)$, (102), and $(2)2\bar{4}$ to validate the crystal structure $[P(o\text{-PDM + m-PDM})]^{TF}$ which appears at in Fig. 7a. According to Calvo and Faggiani [44], the intermolecular interference between nanocomposite chains may account for the strong peaks at (011) and (330) for nanocomposite. Reflection of the *Orthorhombic* symmetry in the space group corresponds to *Pbca(61)*. According to database code amcsd 0000435, this corresponds to the actual value of 2θ, d-spacing and miller index (*hkl*) [45]. Another minor peak appears at (*hkl*) equals to (110), (201), (230), $(\bar{1}\ \bar{2}3)$, (302), (134), (432) and $(\bar{4}04)$ to validate the crystal structure $[P(o\text{-PDM + m-PDM})/ZrO_2]^{NC}$ which appears at in Fig. 7b. Table 2 demonstrated the crystal device variance, *hkl*, d-spacing (d), as well as full-width at half-maximum (FWHM) (β) of the crystalline structure of the manufactured thin film. Fig. 7(a, b) prove that the copolymer and nanocomposites have polycrystalline structure with a *Triclinic group* unit cell with the following characteristics a = 10(2) Å, b = 10(1) Å, c = 10 (1) Å, α = β = γ = 90°, and volume = 3000 (437) $Å^3$. Table 2 indicates that the average crystallite size (D_{Av}) of the $[P(o\text{-PDM + m-PDM})]^{TF}$ and $[P(o\text{-PDM + m-PDM})/ZrO_2]^{NC}$ thin films are 26.21 nm and 56.80 nm, respectively. Because of the well-established relationship between the average crystallite size and the size distribution of a semiconducting material, its properties have long been studied [46]. A wide dispersion spectrum in XRD

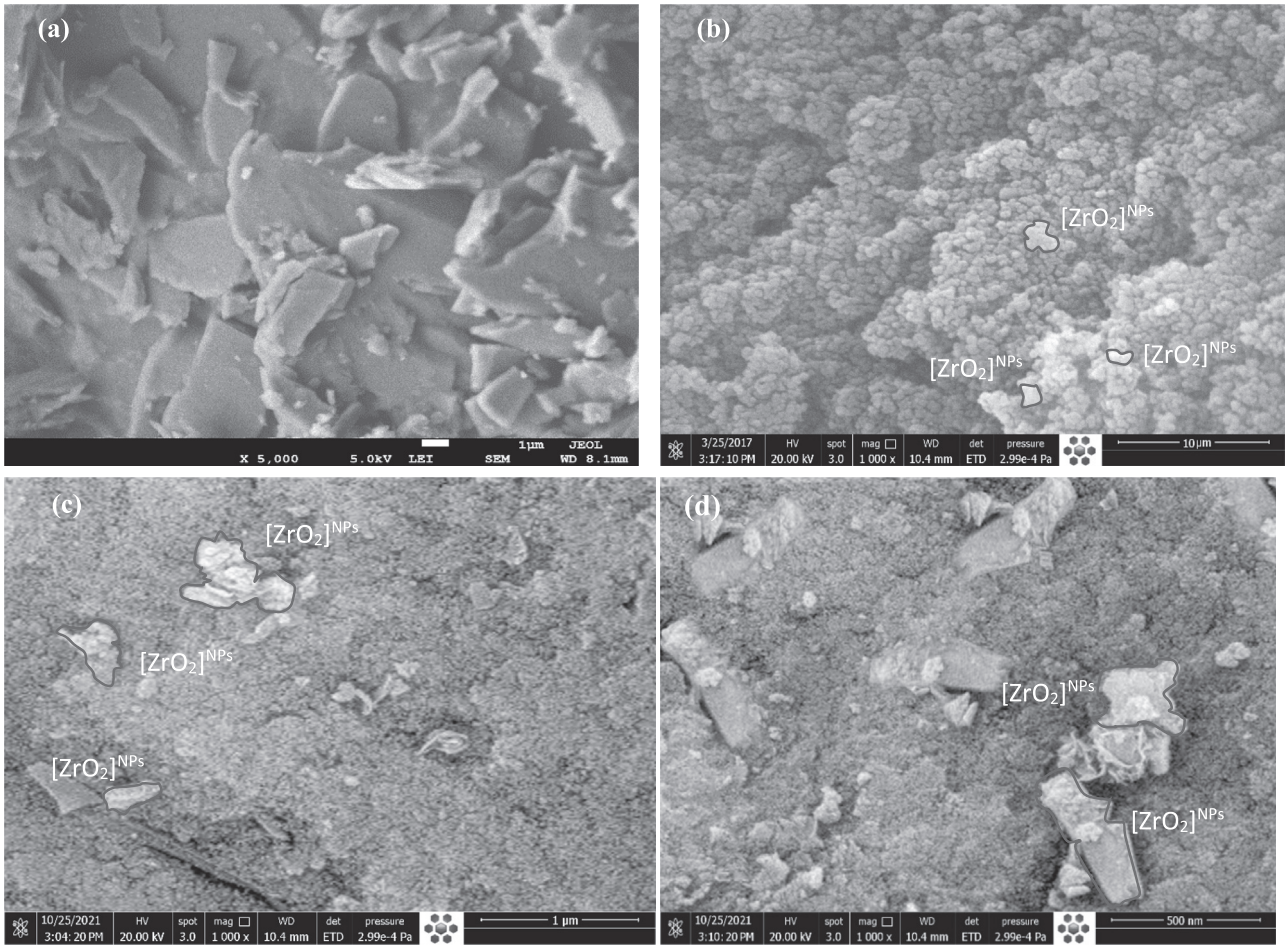

Fig. 5. SEM of a) $[P(o\text{-}PDM + m\text{-}PDM)]^{TF}$ flakes at 1µ magnification and b, c and d) $[P(o\text{-}PDM + m\text{-}PDM)/ZrO_2]^{NC}$ at three different magnifications (5µ, 1µ and 500 nm).

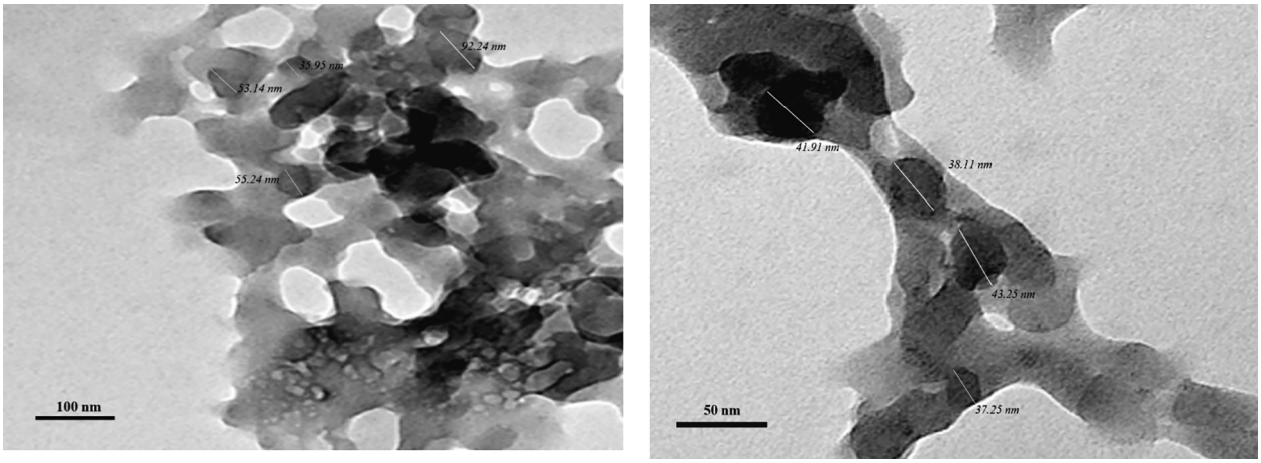

Fig. 6. HRTEM of the $[P(o\text{-}PDM + m\text{-}PDM)/ZrO_2]^{NC}$ thin film.

pattern are dependent especially susceptible to arrangements of atom and crystallite size of particles in unit cell [47]. At $5^0 \leq 2\theta \leq 45^0$, the FWHM (β) and D_{Av} were determined. The interplanar distance (d-spacing) between the greatest diffraction peaks and D_{Av} by Debye–Scherrer is calculated using Bragg's equation: $D_{Av} = 0.9\,\lambda/\beta cos\theta$ where (λ = 0.154 nm), θ is the matching 2θ and the β and FWHM (in radians) [48] are recorded in Table 2.

PXRD patterns of the polymorphs were calculated utilizing the polymorph calculations approach in the *material studio software program (version 7.0)*. A $2 \times 2 \times 1$ matrix was used to calculate

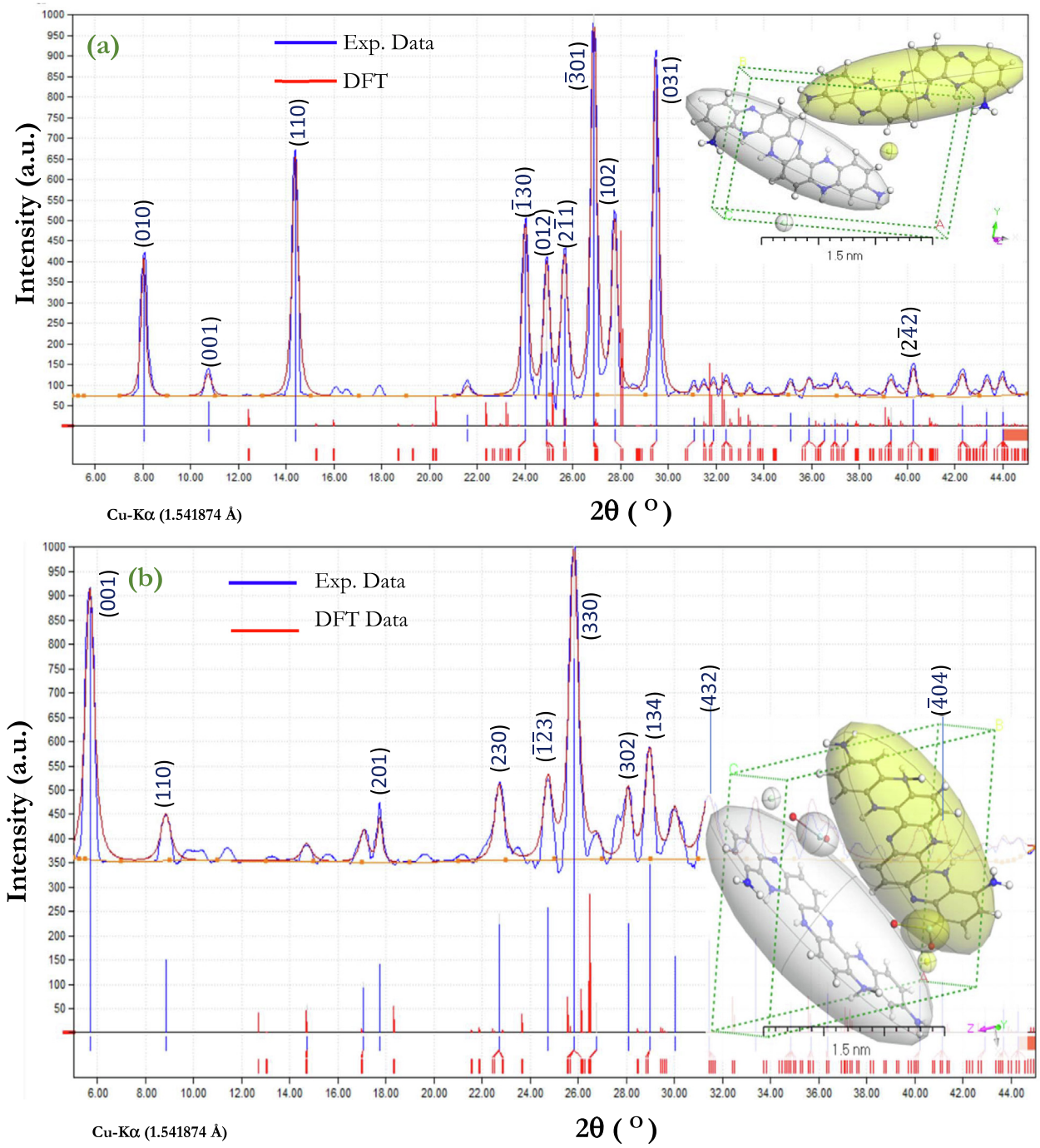

Fig. 7. Combined experimental and simulated PXRD patterns for a) P(o-PDM + m-PDM)^{TF} b) [P(o-PDM + m-PDM)/ZrO_2]^{NC}, inset Figure is a 3D triclinic lattice type using *Polymorph computation method.*

the integrals over the Brillouin zone, as shown in the inset of Fig. 7 (polymorph [P(o-PDM + m-PDM)] and [P(o-PDM + m-PDM)/ZrO_2] as isolated molecules). There are slight changes in the intensities and placements of certain peaks between the experimental and calculated PXRD patterns; however, we will only concentrate on the major areas of similarity between them in this section [49]. Microstructural aspects of powder samples may impact the experimental PXRD pattern in addition to the features of instruments and data collecting methods. This includes crystallite size, shape, and orientation distribution. The observed and anticipated PXRD patterns for both polymorphs match well when compared qualitatively, indicating that the synthesized materials' PXRD patterns are correct [50].

Geometry study for P(o-PDM + m-PDM) and [P(o-PDM + m-PDM)/ZrO_2] as an isolated molecule

In the ground gaseous state, the most stable highest occupied and lowest unoccupied molecular orbitals (HOMO and LUMO) were determined using M062X/6–31 + G(d,p) computations, and presented in Fig. 8. The difference in energy between the fragment molecular orbitals theory (FMOs) determines the equilibrium state of the molecule, which is important for determining the electrical conductivity and grasping electricity transit. Isolated compounds are stable if their entropy values are completely negative [51]. An aromatic compound electrophilic sites may be deduced using the observed FMOs. When dimer molecule bonds (DMB) grew

Table 2
The computing results from the *Refine Version 3.0 Software Program (Kurt Barthelme's and Bob Downs)* for P(o-PDM + m-PDM)[TF] b) [P(o-PDM + m-PDM)/ZrO_2][NC].

Symmetry / Compound	Experimental 2θ	d	*hkl*	Calculated 2θ	d	Difference 2θ	d	FWHM Py[(d)]	FWHM Cm[(e)]	D_{Av} Py[(d)]	D_{Av} Cm[(e)]
Nanocomposite	5.680	15.98	(001)	5.770	15.7	0.09	0.24	0.382	0.055	21.76	151.6
Orthorhombic Pbca(61)	8.850	10.17	(110)	8.630	10.4	−0.22	0.26	0.345	0.114	24.14	73.06
a = 10(2); b = 10(1),	17.73	5.041	(201)	17.83	5.01	0.10	0.03	0.322	0.171	26.10	49.15
and c = 10(1) nm	22.70	3.940	(230)	22.74	3.93	0.04	0.01	0.340	0.181	24.91	46.79
α = γ = β = 90.0°	24.73	3.620	$(1\bar{2}\,3)$	24.73	3.62	0.01	0.00	0.336	0.122	25.30	69.68
V = 3000 (4);	25.81	3.470	(330)	25.76	3.48	−0.04	0.01	0.344	0.228	24.76	37.36
Rmse [(a)] = 0.0081060877	27.91	3.212	(302)	27.87	3.22	−0.03	0.00	0.304	0.228	28.15	37.53
λ = 1.541838 Å[(b)]	28.94	3.099	(134)	28.94	3.10	−0.01	0.00	0.305	0.299	28.12	28.68
ME [(c)]= − 10.846	31.47	2.854	(432)	31.49	2.85	0.02	0.00	0.309	0.458	27.92	18.84
	41.08	2.204	$(\bar{4}\,04)$	41.08	2.20	0.00	0.00	0.287	0.159	30.90	55.77
Average										**26.21**	**56.80**

[(a)] Root mean square error;
[(b)] nm,
[(c)] Machine error,
[(d)] Copolymer P(o-PDM + m-PDM)[TF],
[(e)] Nanocomposite [P(o-PDM + m-PDM)/ZrO_2][NC].

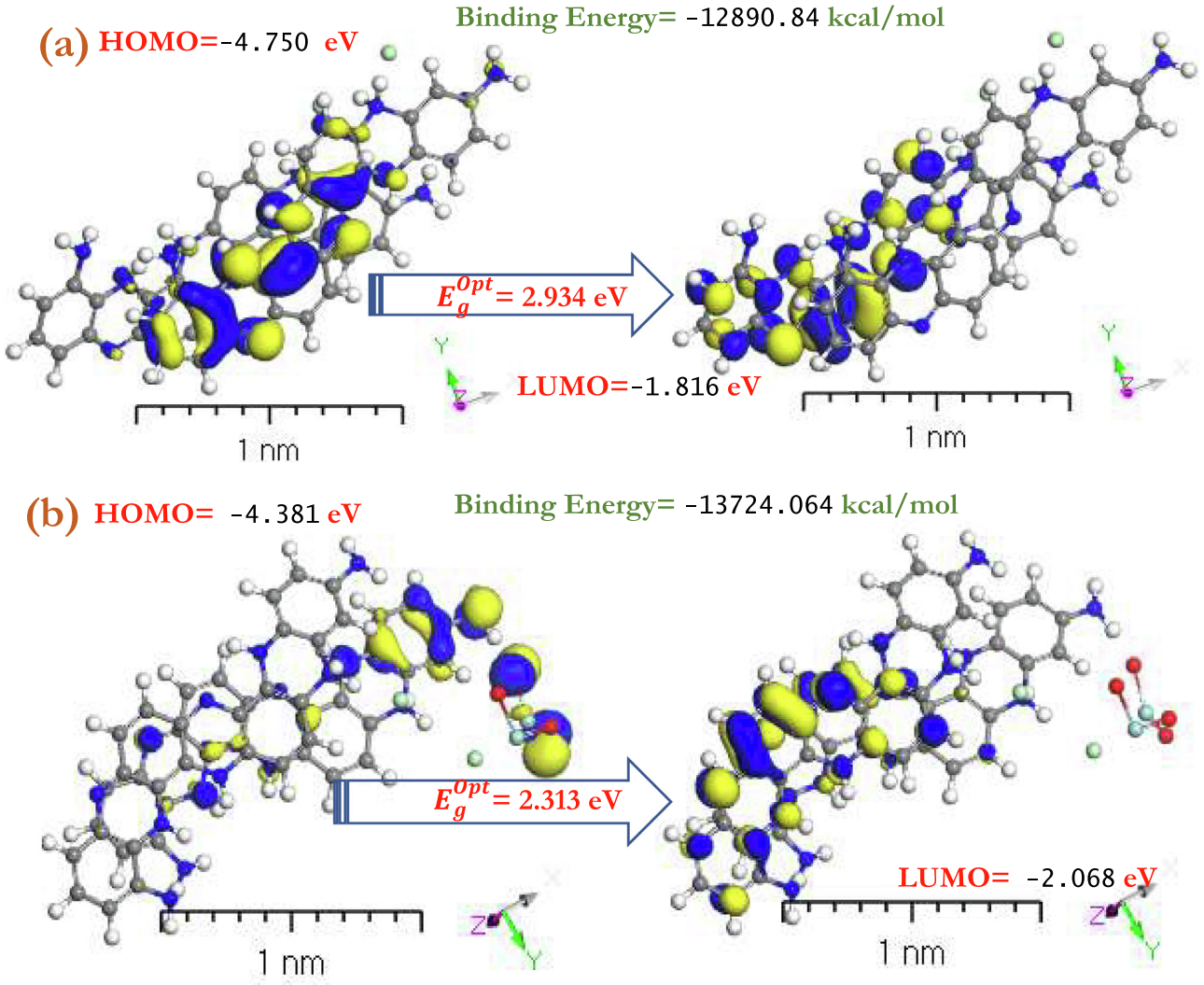

Fig. 8. TD-DFT computations using DMol[3] method for HOMO and LUMO calculations a) P(o-PDM + m-PDM) dimer as an isolated molecule b) the [P(o-PDM + m-PDM)/ZrO_2][NC] dimer molecule.

Table 3
Calculated E_H, E_L, global hardness (η), chemical potential (μ), electronegativity (χ), global softness (S), and global electrophilicity index (ω), ΔN_{max} and σ for P(o-PDM + m-PDM) and [P(o-PDM + m-PDM)/ZrO_2]^{NC} as a dimer and an isolated molecule.

Compound	E_H	E_L	$\Delta E_g^{Opt.}$	χ (eV)	μ (eV)	η (eV)	S (eV)	ω (eV)	ΔN_{max}	σ(eV)$^{-1}$	$(\Delta E_b)^a$
[1]	−4.889	−2.099	−2.309	3.434	−3.434	1.475	0.339	3.998	2.329	0.678	12.956
Dimer	−4.750	−1.816	−2.934	3.283	−3.283	1.467	0.341	3.674	2.238	0.682	-
[2]	−4.401	−2.099	−2.302	3.250	−3.250	1.151	0.434	4.588	2.824	0.869	41.838
Dimer	−4.381	−2.068	−2.313	3.225	−3.225	1.157	0.432	4.495	2.788	0.865	-

[1] = P(o-PDM + m-PDM) and [2] = [P(o-PDM + m-PDM)/ZrO_2]^{NC} and a) kcal/mol.

Table 4
The values of the nonlinear coefficient parameters ($r_1 and r_2$) for [P(o-PDM + m-PDM)]^{TF} and [P(o-PDM + m-PDM)/ZrO_2]^{NC} heterojunction diode.

Temp. (K)	[P(o-PDM + m-PDM)]^{TF}		[P(o-PDM + m-PDM)/ZrO_2]^{NC}		Activation Energy E_g^0 (eV)
	r_1	r_2	r_1	r_2	
298	1.34	1.66	1.81	2.16	$E_g^0[P(oPDM + mPDM)]^{TF} = 2.646eV$
328	1.28	1.53	1.78	2.93	$E_g^0[P(oPDM + mPDM)/ZrO_2]^{NC} = 2.01eV$
358	1.21	1.33	1.67	2.48	
388	1.29	1.25	1.66	2.89	
408	1.47	1.57	1.55	2.35	

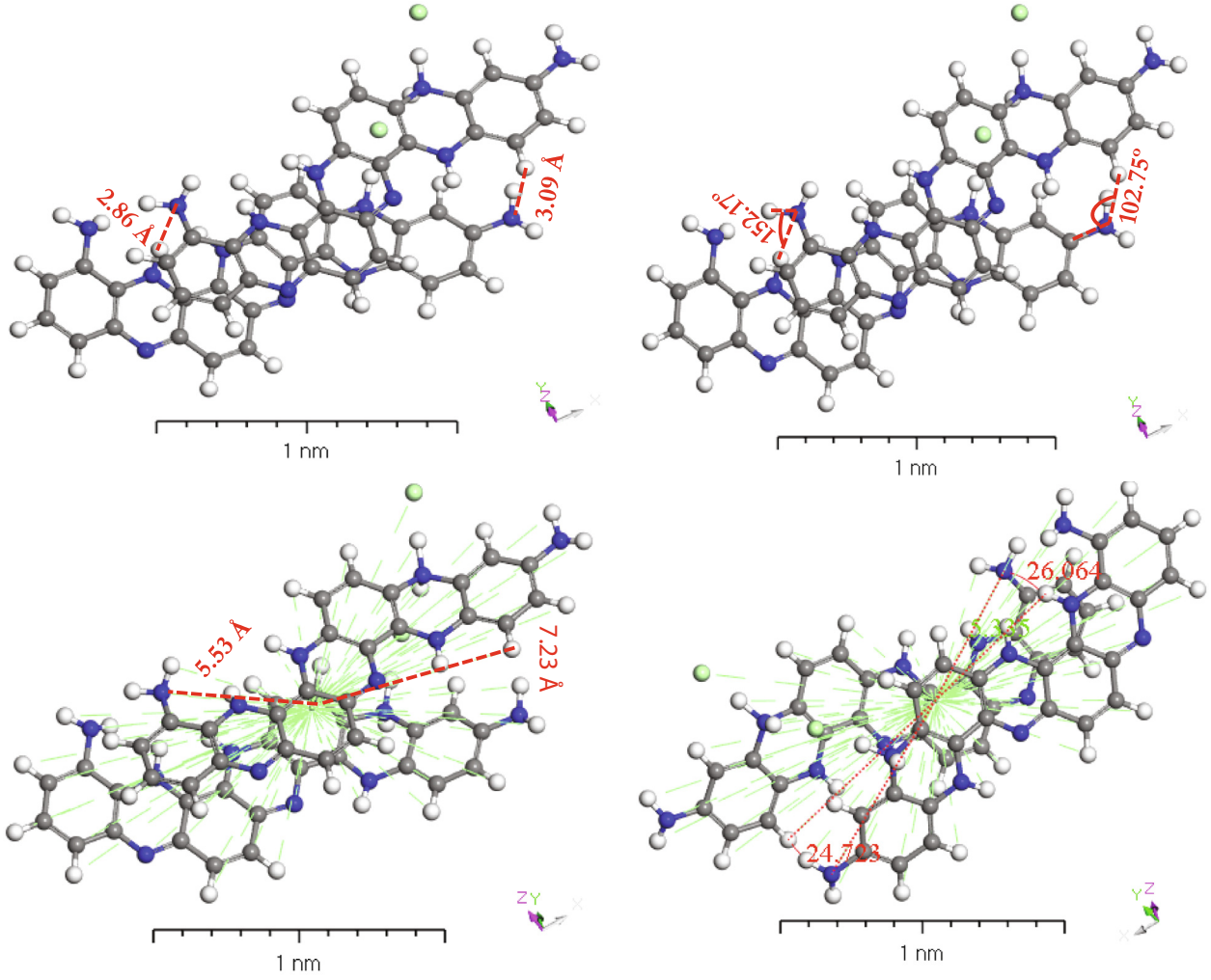

Fig. 9. Stable structures for P(o-PDM + m-PDM) dimers in the gas phase, calculated with B3LYP/6–31 + G(d,p).

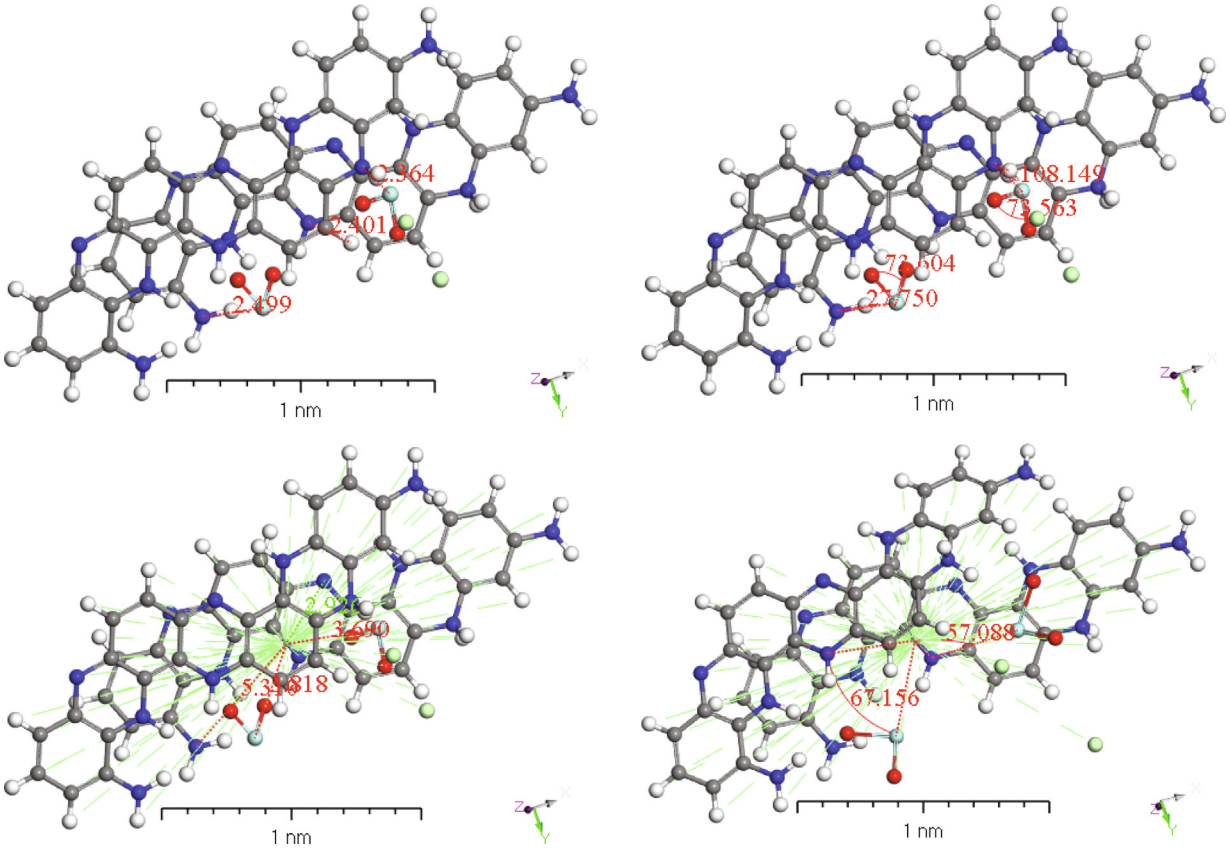

Fig. 10. Stable structures for $[P(o\text{-}PDM + m\text{-}PDM)/ZrO_2]^{NC}$ dimers in the gas phase, calculated with B3LYP/6–31 + G(d,p).

and bond length reduced, the Gutmannat variance technique was used on the DMB sites to enhance the HOMO energy (E_H) [52]. These properties were determined by looking at the optimized energy gap (E_g^{Opt}), as well as the reactivity and stability of the molecular system. Softness and hardness are the most critical factors in determining the stability and responsiveness [40,53]. From the calculated electronegativity equation.

$$(\chi) = (E_H + E_L)/2 \tag{2}$$

and the energy bandgap which explains the link between charge transport in the molecule were demonstrated in Table 3. Table 4..

The HOMO level is frequently found on the benzine ring of copolymer (-C–C = C-) and benzine ring (-C–C = C-) and $[ZrO_2]^{NPs}$ of composite which are prime targets for nucleophilic attack. From Figs. 8 and 9, we observed that HOMO energy of P(o-PDM + m-PDM) and $[P(o\text{-}PDM + m\text{-}PDM)/ZrO_2]^{NC}$ in gaseous state are −4.889 eV and −4.401 eV (which is an extremely large value), respectively. This value indicated that high excitation energies and, high stability for P(o-PDM + m-PDM). On the other hand, the lower value energy LUMO = -2.309 eV and −2.068 eV can be attributed to the more polarizable and softer which concentrated on quinonoid ring for P(o-PDM + m-PDM) and $[P(o\text{-}PDM + m\text{-}PDM)/ZrO_2]^{NC}$ in gaseous state, respectively. Because soft molecules can supply electrons to an acceptor, they are referred to as reactive molecules rather than hard molecules. The most intriguing descriptor is the quantified compounds index electrophilicity (ω). As the device absorbs external electronic charges, it predicts energy stability [54,55].

There were numerous conformers studied for the ground state geometry in quantum-chemical calculations and the conformer with the lowest energy was selected, which was validated by the harmonic vibrational frequency. The dimers binding energies were adjusted for the basis set superposition error using the counterpoise correction technique BSSE. The binding energies of P(o-PDM + m-PDM) dimers and single molecules are −12890.84 and −6438.942 kcal/mol, respectively [56]. On the other hand, the binding energies of $[P(o\text{-}PDM + m\text{-}PDM)/ZrO_2]^{NC}$ dimers and single molecules are −13724.064 and −6882.951 kcal/mol, respectively. Dimers binding energies (ΔE_b) were assessed at the same level of theory using the following formula:

$$\Delta E_b = E_{dimer} - 2E_{monomer} \tag{3}$$

TDDFT/DMOl^3 method was done on the studied molecules and their dimers to get a better understanding of the nature of intermolecular interactions [57]. Figs. 9 and 10 demonstrates the intermolecular interactions in the studied molecule, which include hydrogen bonding, C–H. . .N, and C–H. . .N. The lengths of the hydrogen bond are 2.86 Å and 3.09 Å for C–H. . .N, and C–H. . .N for P(o-PDM + m-PDM) dimers, respectively. The lengths of coordination bonds are 2.449 Å and 2.364 Å between zirconium metal and nitrogen (O = Zr---N-c) for two moieties of polymer for $[P(o\text{-}PDM + m\text{-}PDM)/ZrO_2]^{NC}$. On the other hand, the centroid lengths of the dimer are 5.53 and 7.32 Å for P(o-PDM + m-PDM) dimers, which decreased to 3.69 and 5.34 Å for $[P(o\text{-}PDM + m\text{-}PDM)/ZrO_2]^{NC}$. The intermolecular distance between the two dimers is less than 3.50 Å, preventing the rings of both molecules from temrotating around the single bonds. Whereas the centroid length of the dimer is more than 3.50 Å, the molecule rings rotate around the centroid point [58]. The dihedral angles (Θ)of (C = N----H) for the P(o-PDM + m-PDM) and $[P(o\text{-}PDM + m\text{-}PDM)/ZrO_2]^{NC}$ dimers isolated molecule are $102.75^{\circ} \le \Theta \le 152.17^{\circ}$ and $27.75^{\circ} \le \Theta \le 108.149^{\circ}$, respectively.

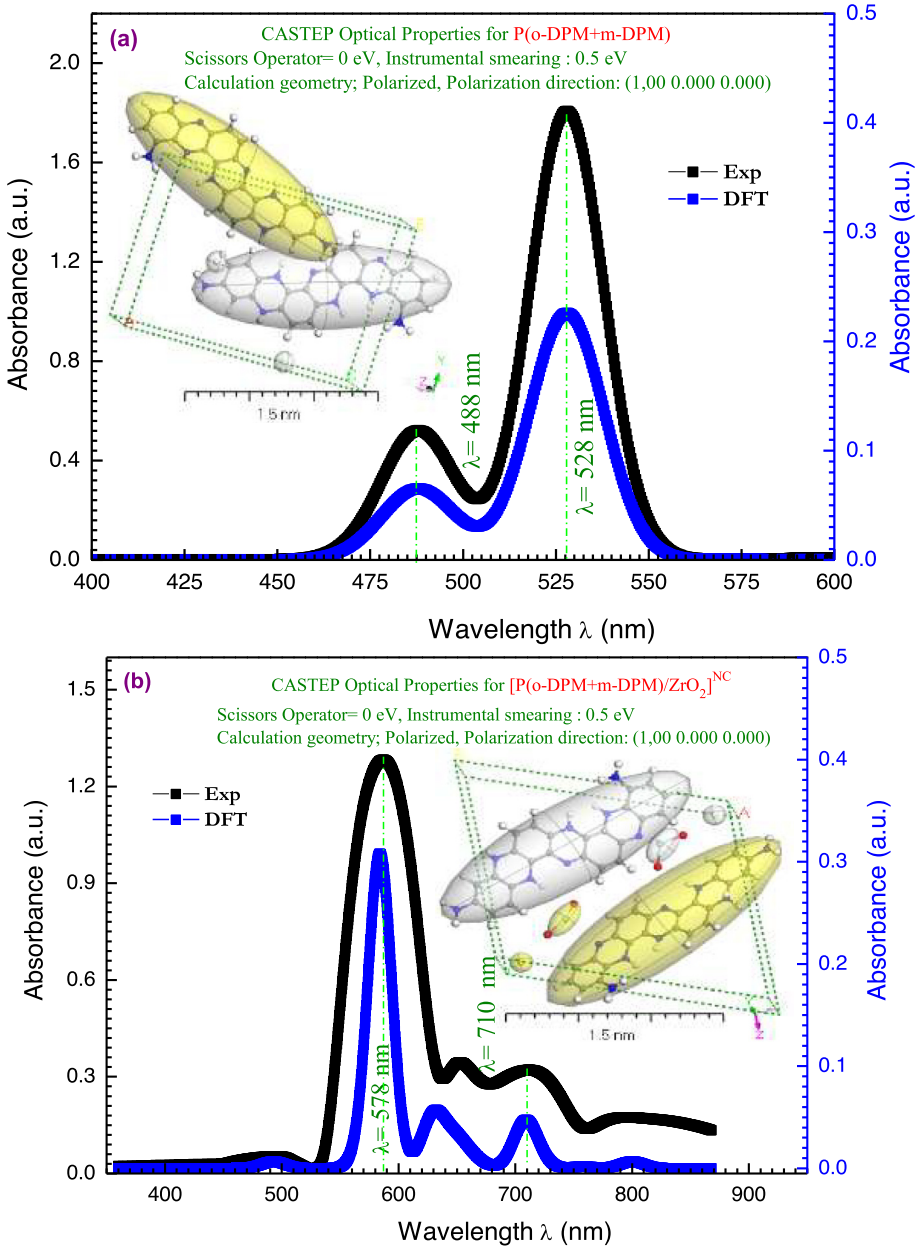

Fig. 11. a) The absorbance spectra of experimental, TD-DFT calculations and 3D molecule for (o-PDM + m-PDM). b) The absorbance spectra of experimental, TD-DFT calculations and 3D molecule for [P(o-PDM + m-PDM)/ZrO_2]^{NC}.

Optical properties of [P(o-PDM + m-PDM)] and [P(o-PDM + m-PDM)/ZrO_2]^{NC}

Understanding the basic absorption edge in the UV region is critical to our films transition and band structure. Fig. 11(a, b) indicates the recorded experimental absorption spectra of the thin films (o-PDM + m-PDM)^{TF} and [P(o-PDM + m-PDM)/ZrO_2]^{NC} where two bands at 528 and 587 nm as main peak, and 488 nm and 710 as minor peak were observed. As can be observed, absorption reduces significantly as the UV wavelength increases. This drop might be due to the observed decrease in the crystallinity of the films in this condition [59]. The TD-DFT analysis was used to examine the theoretical optical response of (o-PDM + m-PDM) and [P(o-PDM + m-PDM)/ZrO_2]^{NC} as an isolated molecule at 300 > λ (nm) > 900. The TD-DFT/CASTEP findings were used to compare the absorption bands of the fabricated thin films with a thickness of 100 ± 5 nm developed at 298 K is indicated in Fig. 11 (a, b). The theoretical and experimental photo-absorption spectrum showed a main absorption at 528 nm for (o-PDM + m-PDM) and 578 nm for [P(o-PDM + m-PDM)/ZrO_2]^{NC} attributed to π–π* electronic transitions in phenylene diamine matric structure.

The indirect ($E_{Indir}^{Opt.}$) and direct ($E_{Dir}^{Opt.}$) optical bandgaps of the film were studied by means of the Tuac's relation:

$$(\alpha h\nu)^{\psi} = \beta(h\nu - E_g^{Opt.}) \quad (4)$$

where (β) is a constant, ($h\nu$) is the incident energy, and ($\psi = 0.5 and 2$) for the indirect and direct allowed transitions, respectively. ($E_g^{Opt.}$) is estimated from the straight portion of $(\alpha h\nu)^2$ versus ($h\nu$) plot at $\alpha = 0$, as shown in Fig. 12. As can be seen, ($E_{Dir}^{Opt.}$) of (o-PDM + m-PDM) and [P(o-PDM + m-PDM)/ZrO_2]^{NC} thin films are 2.29 and 1.98 eV, respectively. The change in ($E_g^{Opt.}$) can be explained by the creation of charge transfer between functional

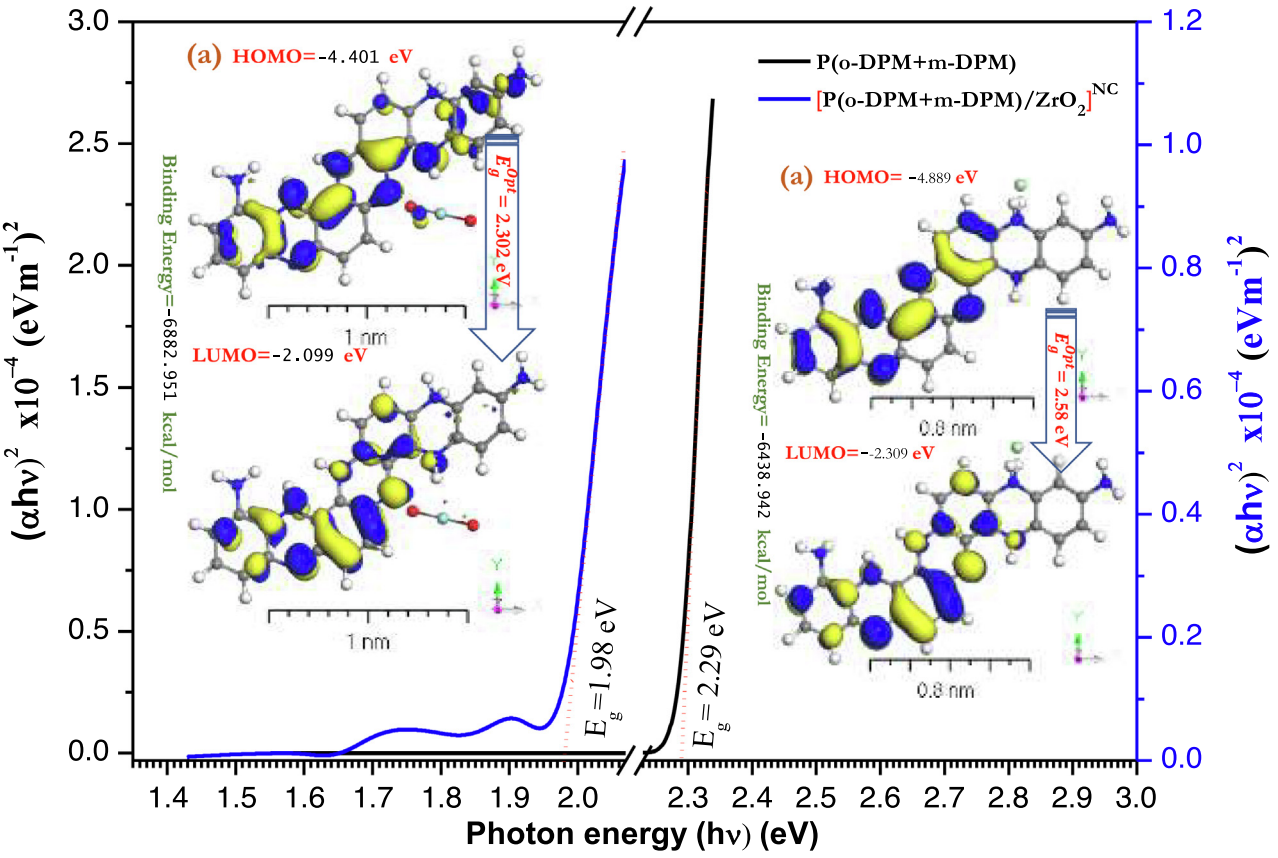

Fig. 12. The relationship of photon energy with electronic transitions for (o-PDM + m-PDM) and [P(o-PDM + m-PDM)/ZrO_2]^{NC}. Inset figure is a schematic diagram of theoretical calculations of energy gap using TD-DFT/DMol^3 method for the isolated molecule.

groups of ($E_{Dir}^{Opt.}$) with the amide groups which was reported in previous work [60]. The energy gap between HOMO and LUMO ($\Delta E_g^{Opt.} = E_H - E_L$), electronic energy, dipole moment, and the maximum absorption wavelength (λ_{abs}) calculated in the gas phase with M062X/6–31 + G(d,p) and experimental results are presented in Fig. 12. $\Delta E_g^{Opt.}$ between the two molecular orbitals in the gas phase is comparable to that measured experimentally, which accounts for the similarity in the estimated absorption spectra, suggesting that the TD-DFT functional reproduces the experimental values more accurately [61,62].

When the experimental technique is compared to the theoretical method (GGA-PW91 functional) for the [P(o-PDM + m-PDM)/ZrO_2]^{NC} moiety, a good agreement is found [63]. The relationship between the extinction coefficient "k(λ)" of the films and the absorption (Abs.) spectra is as follows:

$$k = \alpha\lambda/4\pi \tag{5}$$

The absorption coefficient $(\alpha) = Abs./d$ where d is the film thicknesses. As observed in Fig. 13, the [P(o-PDM + m-PDM)/ZrO_2]^{NC} thin film exhibits the highest absorption value in most of the considered wavelength range. This band is therefore characteristic of [P(o-PDM + m-PDM)/ZrO_2]^{NC} thin film and is attributed to the π–π* transitions generated by the unsaturated bonds [33]. On comparing the experimental and TD-DFT/CASTEP simulated technique, a good similarity was obtained. On the other hand, the value of k(λ) less than the refractive index "n(λ)" with a molar ratio equal to $n(\lambda)/k(\lambda) = 9.5 \times 10^7$. This result indicates that k(λ) is the key structural parameter controlling many canopy functions like radiation and water interception, radiation extinction, and water and gas exchange [64]. The interception between refractive index n (λ) and extinction coefficient k(λ) of [P(o-PDM + m-PDM)/ZrO_2]^{NC} thin film gave the value of energy gap = 1.99 eV.

The frequency dependence of the optical dielectric constant is a parameter that provides information about the electronic excitations within the material. The real (ε_{Re}) and imaginary (ε_{Imag}) parts of the dielectric constant were determined by the following equations [65]:

$$\varepsilon_1 = n(\lambda)^2 - k(\lambda)^2 \tag{6}$$

and.

$$\varepsilon_2 = 2n(\lambda)k(\lambda) \tag{7}$$

It is seen, from Fig. 14a, that with increasing photon energy, the ε_{Re} and ε_{Imag} values increase and then decrease at the higher values of photon energy ($h\nu = 0eVand5eV$). The maximum values of ε_1 and ε_2 are 2.93 and 5.56 × 10^{-8} at $h\nu = 1.8eVand2.20eV$ for the [P(o-PDM + m-PDM)/ZrO_2]^{NC} thin film, respectively. Using the CASTEP technique, the maximum value of $\varepsilon_1(\lambda)$ and ε_2 (λ) in the isolated state is ≅ 1.80 at various frequencies (eV) ≅ 0–5, as shown in Fig. 14b. The average values of $\varepsilon_1(\lambda)$ and $\varepsilon_2(\lambda)$ derived from the experimental and simulation dimensions fall between 1–5 eV in frequency [66]. From the behavior of the simulated [P(o-PDM + m-PDM)/ZrO_2]^{NC} as an isolated molecule in Fig. 10b, the CASTEP/DFT calculations were utilized to assess $\varepsilon_1(\lambda)$ and $\varepsilon_2(\lambda)$ and compared to the experimental values are close to those achieved by TD-DFT with the CASTEP model.

The optical conductivity real $\sigma_1(\lambda)$ and imaginary $\sigma_2(\lambda)$ parts are calculated from [67]:

$$\sigma_1(\omega) = \omega\varepsilon_2\varepsilon_0 \tag{8}$$

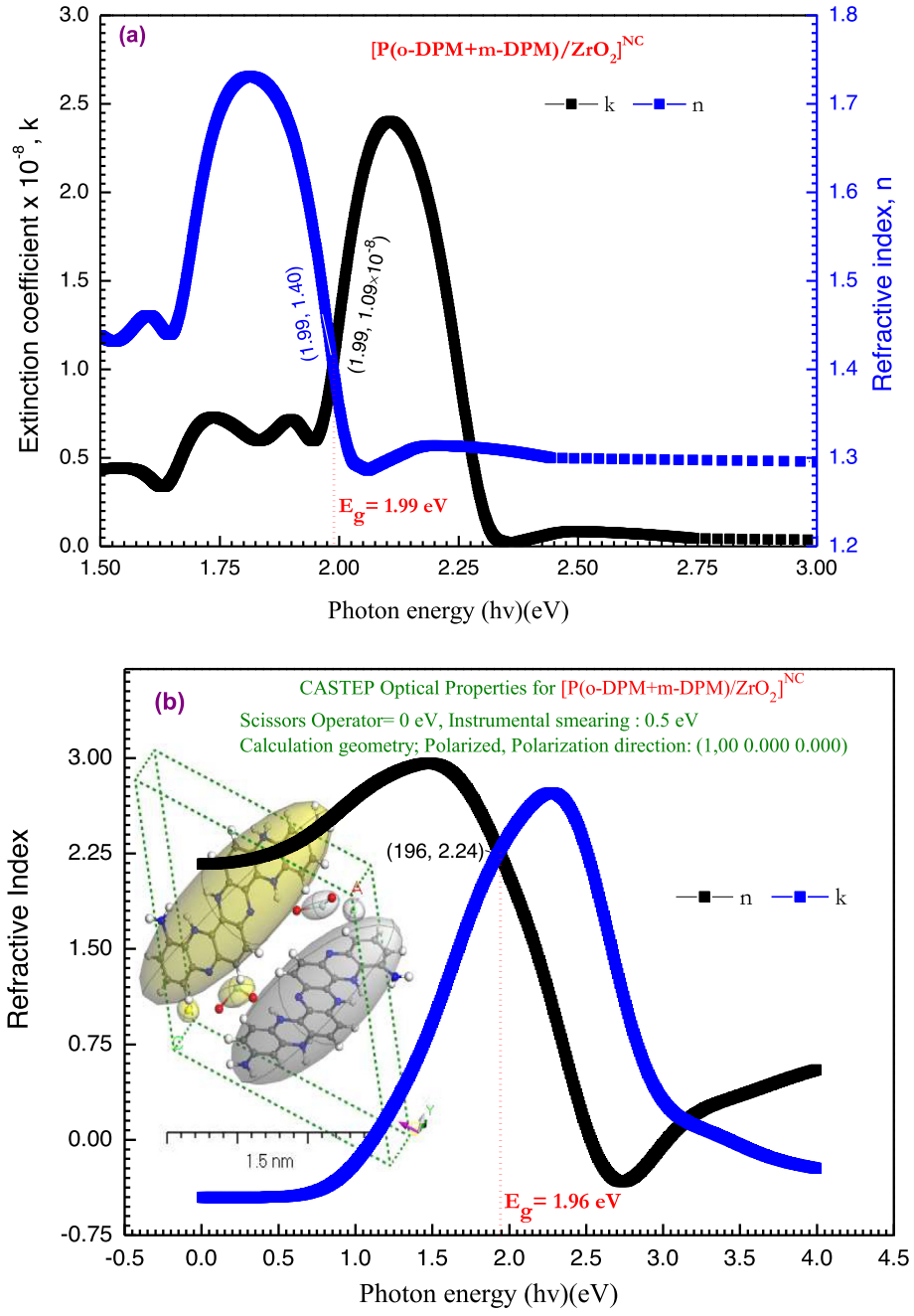

Fig. 13. a) The refractive index n(λ) and extinction coefficient k (λ) of [P(o-PDM + m-PDM)/ZrO_2]^{NC} thin film. b) The simulated computation of (n) and (k) for [P(o-PDM + m-PDM)/ZrO_2]^{NC} as isolated molecule by using CASTEP/DFT and inset Fig is lattice type: 3D Triclinic by using polymorph computation method.

and.

$$\sigma_2(\omega) = \omega\varepsilon_1\varepsilon_0 \tag{9}$$

where the real part $\sigma_1(\lambda)$ represents the in-phase current, while the imaginary part $\sigma_2(\lambda)$ represents the $\pi/2$ out-of-phase inductive current, ω is the angular frequency (ω = 2πν), ε_0 is the free space dielectric constant, $\varepsilon_1(\lambda)$ is the real (normal) dielectric constant, and $\varepsilon_2(\lambda)$ is the imaginary (absorption associated with radiation by free carrier) parts of the dielectric constants. $\varepsilon_1(\lambda)$ and $\varepsilon_2(\lambda)$ are given by [68].

$$\varepsilon_1(\lambda) = n(\lambda)^2 - k(\lambda)^2 \tag{10}$$

and.

$$\varepsilon_2(\lambda) = 2nk \tag{11}$$

The dependence of $\sigma_1(\lambda)$ and $\sigma_2(\lambda)$ on the incident photon frequency ($h\nu$) is displayed in Fig. 15. The values of the imaginary part are larger than that of the real part of optical conductivity by a factor of $\sigma_2(\lambda)/\sigma_1(\lambda) = 7.65 \times 10^7$. The values of $\sigma_1(\lambda)$ and $\sigma_2(\lambda)$ are slightly increased with the photon energy increasing. At $h\nu = 2.75$ eV, the conductivity is nearly decrease with increase the photon energy. After that, it increases sharply near the UV region due to the strong interaction between the highly energetic photons and the charge carriers of the material.

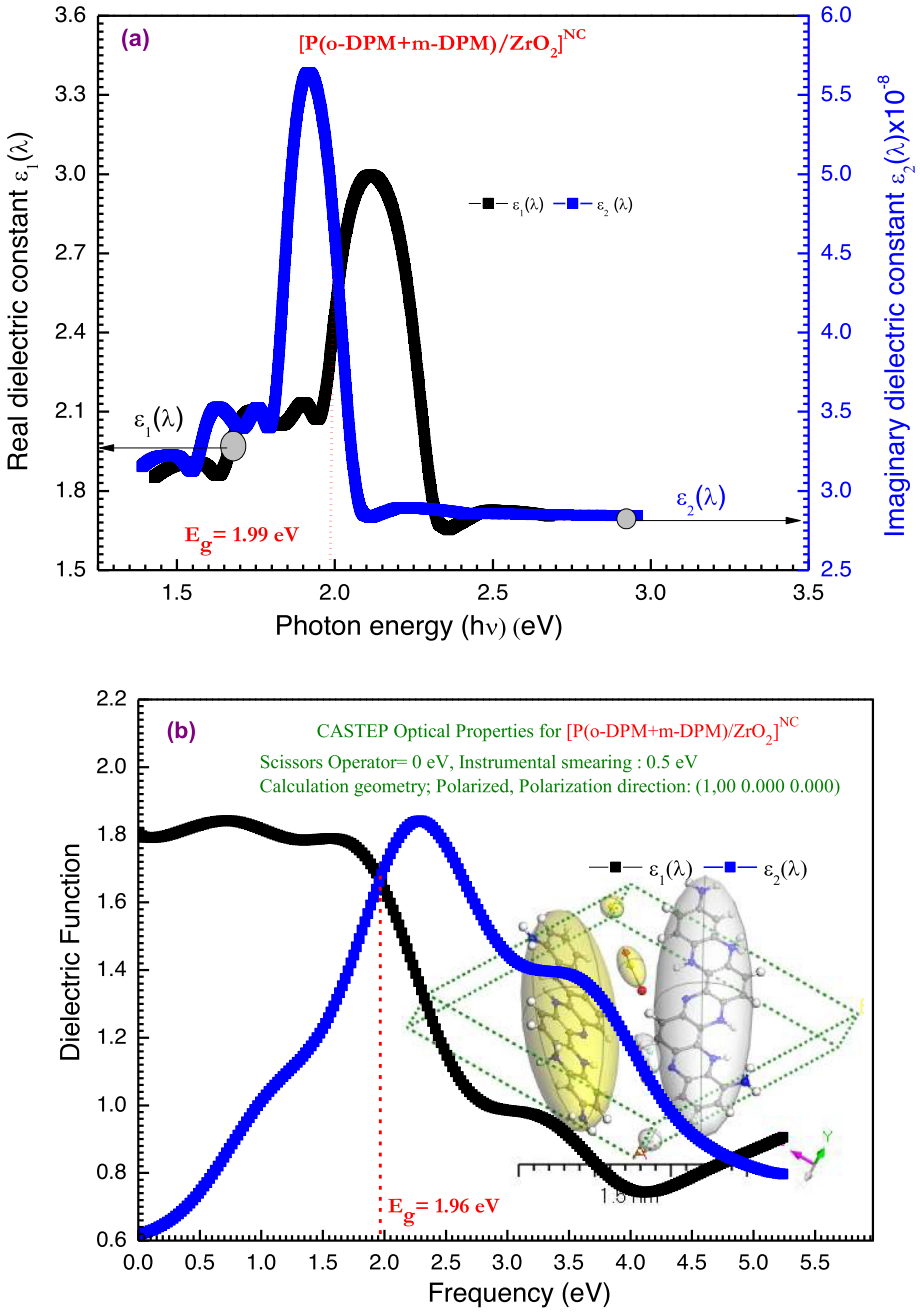

Fig. 14. a) The experimental $\varepsilon_{Re}(\lambda)$ & $\varepsilon_{Imag}(\lambda)$ for [P(o-PDM + m-PDM)/ZrO_2]^{NC} thin film. (b) Simulated $\varepsilon_{Re}(\lambda)$ & $\varepsilon_{Imag}(\lambda)$ for [P(o-PDM + m-PDM)/ZrO_2]^{NC} as an isolated state using the CASTEP method. Inset Fig is lattice type: 3D Triclinic by using polymorph computation method.

Photoluminescence behavior

The photophysical properties of the [P(o-PDM + m-PDM)]^{TF} and [P(o-PDM + m-PDM)/ZrO_2]^{NC} thin films were investigated, Fig. 16 (a, b). As seen in Fig. 16a, exciting the copolymer and nanocomposite at 450 nm resulted in the emission at two main regions with λ_{max} = 477, and 536 nm. The thin film of [P(o-PDM + m-PDM)]^{TF} and [P(o-PDM + m-PDM)/ZrO_2]^{NC} showed emission spectra (Fig. 16a) to give Commission Internationale de l'Eclairage (CIE) chromaticity coordinates of (x, y) = (0.14, 0.16) and (0.18, 0.23), respectively, producing blue-white color. When the excitation spectra of the [P(o-PDM + m-PDM)]^{TF} thin film is compared with [P(o-PDM + m-PDM)/ZrO_2]^{NC} thin film, a considerable difference can be seen, indicating that aggregation has a significant impact on the excited state, and generated, red-shifted emission bands, due to the creation of - interactions between the generated aggregates, this is typical of copolymer and nanocomposite luminous materials. To further confirm the aggregation-induced emission (AIE) characteristic of the investigated copolymers and nanocomposite materials, the photoluminescence of the varied thin films [P(o-PDM + m-PDM)]^{TF} and [P(o-PDM + m-PDM)/ZrO_2]^{NC} with the same thickness were investigated. The observed Stokes shifts.

$$\Delta = \lambda_{Emission} - \lambda_{Excitation} \quad (12)$$

was computed as ≅ 17 nm and 27 nm, for [P(o-PDM + m-PDM)]^{TF} and [P(o-PDM + m-PDM)/ZrO_2]^{NC}, respectively. It is possible to compare the excitation and absorption spectra, and both forms are mirror images of one another. Excitation spectra were found to be somewhat redshifted in terms of wavelength when compared to the absorption spectra. Both thin films emitted blue light with a CIE value of y 0.3, which was similar to each other. Therefore, the investigated made copolymer and nanocomposite

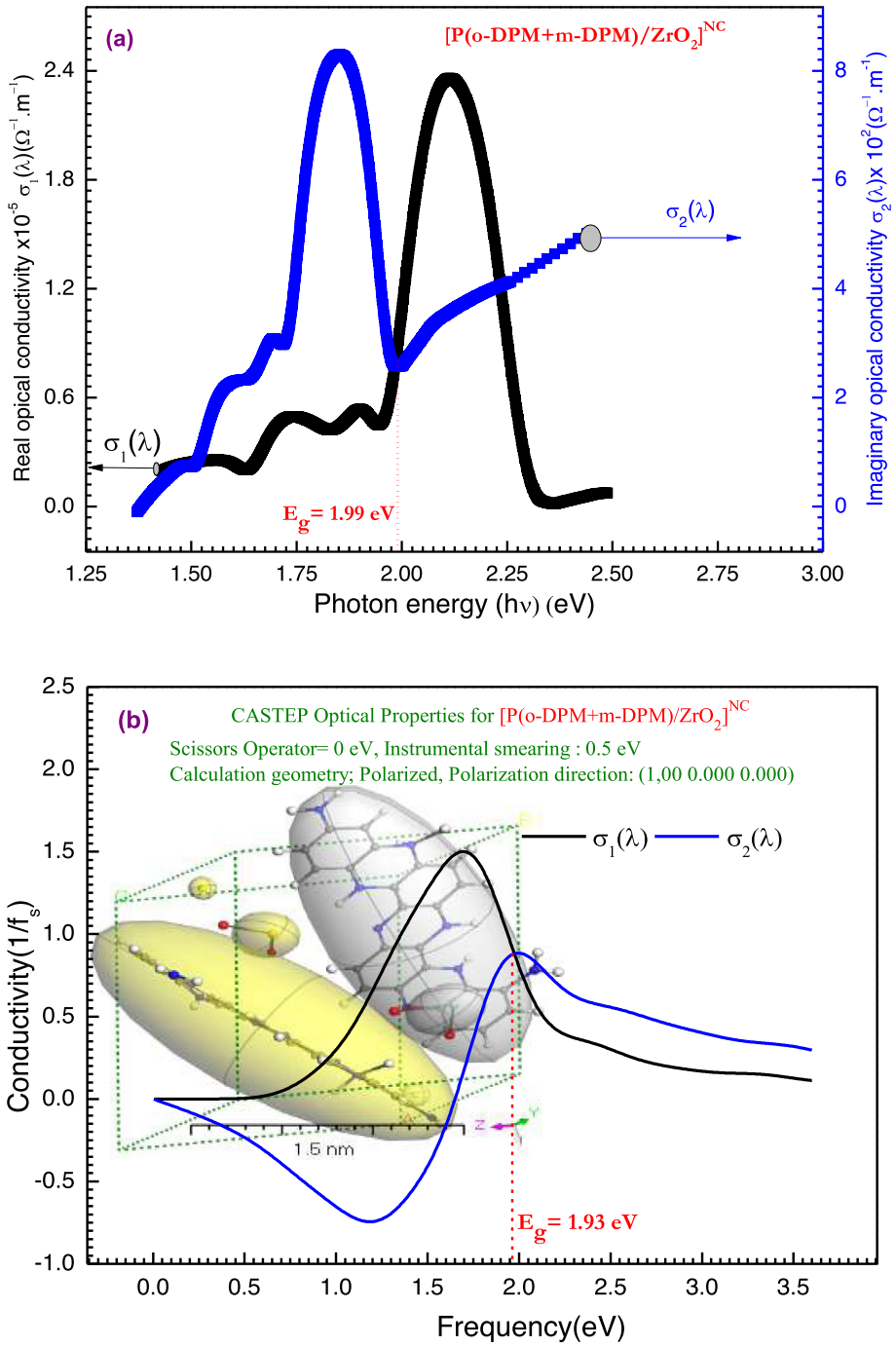

Fig. 15. (a) The experimental $\sigma_1(\lambda)$ and σ_2 (λ) for [P(o-PDM + m-PDM)/ZrO_2]^{NC} thin film. (b) Simulated $\sigma_1(\lambda)$ and $\sigma_2(\lambda)$ as an isolated state using the CASTEP method.

may be characterised as essential luminogens since they emit white light from a [P(o-PDM + m-PDM)/ZrO_2]^{NC} and deep blue light from their [P(o-PDM + m-PDM)]^{TF}, respectively [69,70].

Electrical properties

The effect of [ZrO_2]^{NPs} and heating on DC conductivity for [P(o-PDM + m-PDM)]^{TF}

The [ZrO_2]^{NPs} play a significant role in the creation of polymer nanocomposites, which are crucial in the field of nanotechnology, It is defined as the concentration of filler at which electrical conductivity suddenly increases by several orders of magnitude, indicating that percolation has occurred [71]. The homogeneous distribution of nanoparticles improves the electrical properties of copolymer nanocomposites thin films. Due to the low interfacial contact between [ZrO_2]^{NPs} and polymeric mixtures, as well as the attraction between [ZrO_2]^{NPs} induced by the van der Waals force, which leads [ZrO_2]^{NPs} to aggregate, obtaining such a distribution is difficult [72]. SEM images indicated that the [ZrO_2]NPs produced in this research demonstrated uniform dispersion, which was confirmed by the results of the experiment. The direct conductivity (σ_{dc}) value is shown as a function of temperature T(K) at a constant voltage of 20 V. Charge transfer inside nanocomposite [P(o-PDM + m-PDM)/ZrO_2]^{NC} thin film is enhanced by the interaction of [P(o-PDM + m-PDM)]^{TF} with [ZrO_2]^{NPs}. The σ_{dc} of [P(o-PDM + m-PDM)]^{TF} and [P(o-PDM + m-PDM)/ZrO_2]^{NC} thin films

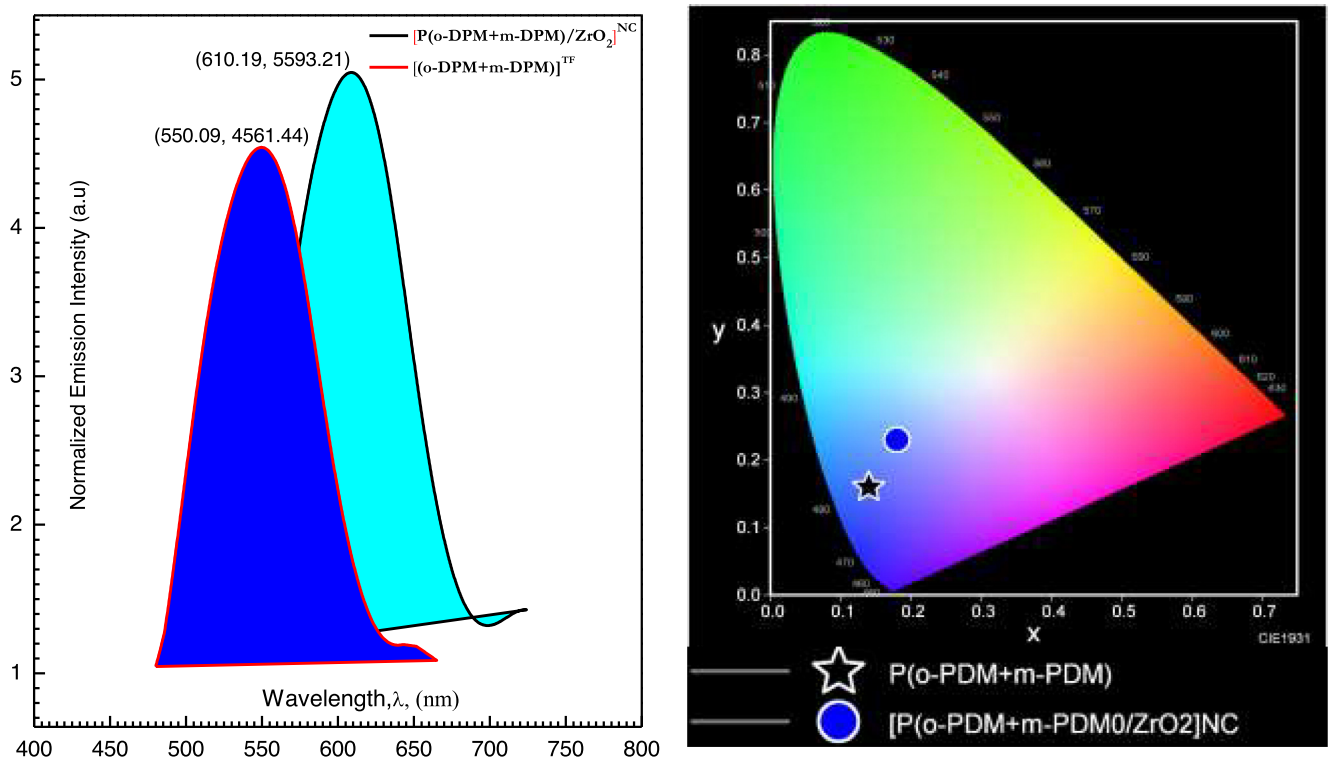

Fig. 16. (a, b) the normalized emission with wavelength and the CIE chromaticity diagrams of the emission colors obtained for [P(o-PDM + m-PDM)]^{TF} and [P(o-PDM + m-PDM)/ZrO_2]$^{NC.}$

Table 5
Au/[P(o-PDM + m-PDM)/ZrO_2]^{NC} /p-Si/Al /p-Si/Al nanocomposite device performances under different illumination intensities..P_{in}

Illumination power[a]	$(V_m)^b$	$(J_m)^c$	$(V_{OC})^b$	$(J_{SC})^d$	Power	FF (%)	η (PCE)
60	19.75×10^{-4}	1.52×10^{-4}	91.61×10^{-4}	1.49×10^{-4}	30×10^{-3}	21.96	5.00
120	23.90×10^{-4}	2.80×10^{-4}	111.52×10^{-4}	1.60×10^{-4}	6.68×10^{-3}	37.43	5.57
240	49.98×10^{-4}	4.36×10^{-4}	185.41×10^{-4}	2.07×10^{-4}	2.18×10^{-2}	56.72	9.07

a= ($W.cm^{-2}$), b = Volt, c= ($mA.cm^{-2}$), and d= ($mA.cm^{-2}$).

are 37.79 × 10^{-5} and 49.75 × 10^{-5} S m^{-1}, respectively, which are higher than the stated value for the free copolymer following E_g^0 values (see Table 5).

By choosing the proper applied electrical field E(V), the [ZrO_2]-^{NPs} may be oriented to reduce agglomeration and extend networks from the negative electrode to the positive electrode. It is advised that the following phases be followed while designing conducting pathways: To begin, the [ZrO_2]^{NPs} are rotated to a certain angle owing to the applied E(V), which forms a dipole moment at their edges, aligning them in the direction of the applied E(V). As a consequence of this attraction, the [ZrO2]NPs attract one another until they come into direct touch, leading in the formation of three-dimensional networks. [ZrO_2]^{NPs} migrate to and stick to the negative electrode in the final step. In conclusion, [ZrO_2]^{NPs} electronic conductivity is the dominant source of (σ_{dc}) in nanocomposite films, while their ionic conductivity is insignificant. As seen in Fig. 17, increasing T(K) (i.e., semiconducting characteristic) results in an increase in charge transfer. Although no three-dimensional networks are formed in the case of copolymers and at lower [ZrO_2]^{NPs} ratios, the energy absorbed by charge carriers activates them to overcome potential barriers [73]. On the other hand, heating will assist in the optimization of these routes by raising their (σ_{dc}) value as the [ZrO_2]^{NPs} content and network growth increase.

The influence of applied potential difference (V) on the current (I)

At T = 298 K and the different illumination 60 ≤ *Illuminations* ≤ $375 mW/cm^{-2}$, the potential bias (V) and logarithms of -log (J) are demonstrated in Fig. 18. The nonlinear coefficient parameter (r) may come from the relationship [74].

$$I = RV^r \tag{13}$$

where R is the constant, and r is the slope of these curves. In (I-V) curves, there are two distinct areas: the (r_1) values for lower (V) and the (r_2) values for higher (V), with (r_2) > (r_1). The nonohmic behaviour of the (I-V) characteristics of the studied films is confirmed by the values of (r_1) and (r_2), which are shown in Table 5 of the results. For Au/[P(o-PDM + m-PDM)/ZrO_2]^{NC}/p-Si/Al heterojunction diode, the nonlinear coefficient parameters are (r_1) and (r_2), with the (r_1) values being less than 2, while the values of (r_1) and (r_2) rising when the temperature of Au/[P(o-PDM + m-PDM)/ZrO_2]^{NC}/p-Si/Al heterojunction diode is increased. When increasing T(K), the (r_1) values are increased. On the other hand, the (r_2) values decrease as the temperature increases. In polymers, the nonlinear coefficient parameters (r) are used to express the conduction process. When ($r = 1$), we have ohmic behaviour. In this case, trap-free space charge incomplete dominates. The trap charge mechanism is faulty if r is greater than 2. Traps become big-

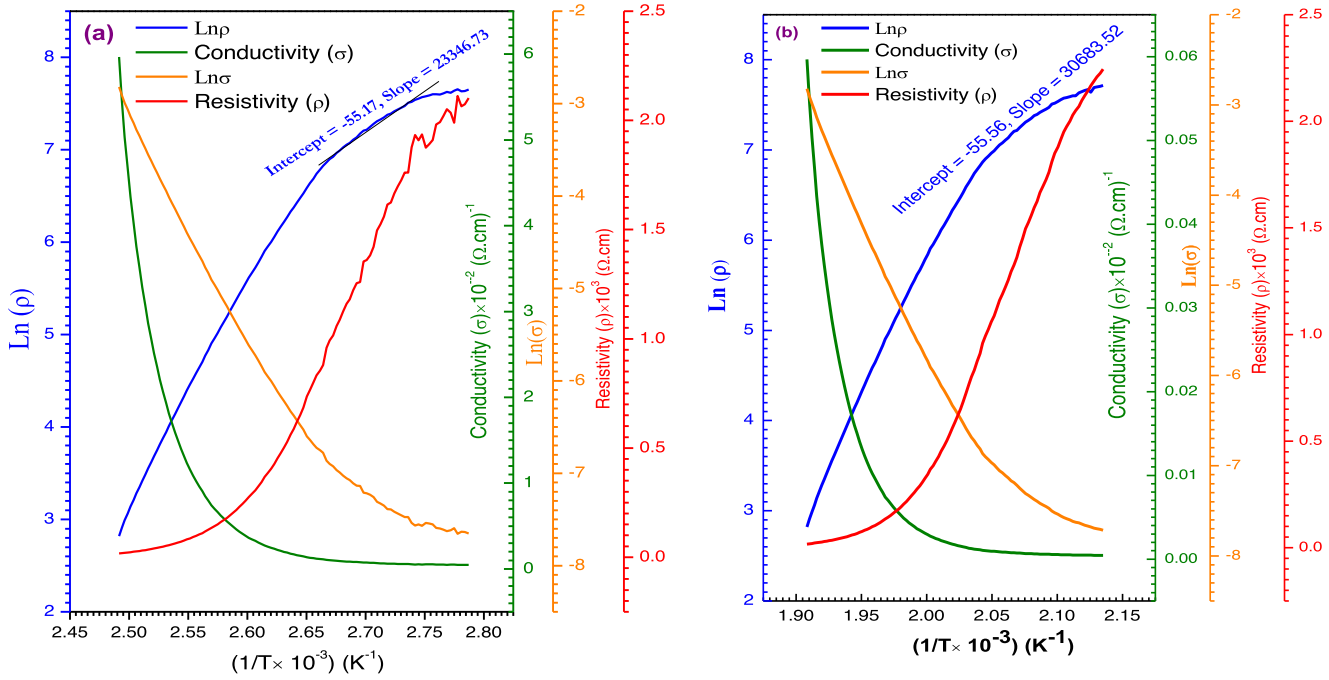

Fig. 17. The dependence of DC resistivity and conductivity of $[P(o\text{-}PDM + m\text{-}PDM)]^{TF}$ and $[P(o\text{-}PDM + m\text{-}PDM)/ZrO_2]^{NC}$ thin films on temperature (1/T).

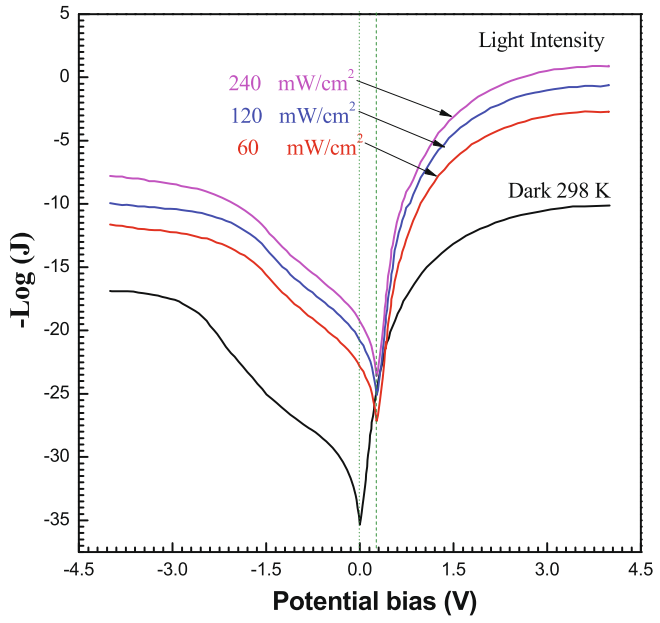

Fig. 18. -log (J) – (V) characteristics curves for $Au/[P(o\text{-}PDM + m\text{-}PDM)/ZrO_2]^{NC}$ /p-Si/Al heterojunction diode under dark with T = 298 K and the different illumination $60 \leq Illuminations \leq 375 mW/Cm^{-2}$.

ger or deeper as r increases. The higher the (V) value, the more $[ZrO_2]^{NPs}$ aggregation is likely to occur, which is undesirable and a concern.

Photovoltaic properties of Au/[P(o-PDM + m-PDM)/ZrO$_2$]^{NC}/p-Si/Al heterojunction diode films

The photovoltaic properties of $Au/[P(o\text{-}PDM + m\text{-}PDM)/ZrO_2]^{NC}$ /p-Si/Al nanocomposite solar cell were performed under various light intensities $60 \frac{mW}{cm^2} \leq P_{in} \leq \frac{240 mW}{cm^2}$. The current–voltage (I–V) properties of the films are measured using a computerized Keithley 2635A system source meter. A GPIB/USB cable was used to connect it to the host computer. At zero voltage and zero current density, the photovoltaic performance of the constructed solar cell was tabulated in Table 6, which included the existence of current density (J_{sc}) and voltage (V_{oc}). (J_{SC}) and (V_{OC}) levels increase as a result of increasing light intensity.

There is an obvious photovoltaic response in the device made of $Au/[P(o\text{-}PDM + m\text{-}PDM)/ZrO_2]^{NC}$/p-Si/Al heterojunction. Since it displays rectified ($J - V$) characteristics (Fig. 18) with the same orientation, but with substantially greater rectification degrees (i.e., ratios between forwarding and backward currents). By raising the (J_{sc}) in proportion to the light intensity using the following equation:

$$J_{sc} = AP_{in}^{\gamma} \quad (14)$$

where A is a constant. The correlation between the current density (J_m) and the voltage (V_m) is the power density (maximum value PM). In Table 6, we computed and displayed the corresponding current density and voltage. As the light intensity rises, the PM, (J_m), and (V_m) readings increase. The fill factor (FF) and efficiency of the device's power conversion (η) were then calculated using the formula [75]:

$$(FF = V_m J_m / V_{OC} J_{SC}) \quad (15)$$

and.

$$(\eta = V_{OC} \times J_{SC} / P_{in} \times FF \times 100) \quad (16)$$

Table 6 contains the values of FF and. Increased light intensity enhances efficiency. Fill factors and efficiency were found to be 56.72% and 9.07%, respectively, at 240 mW/cm^2. A substantial polarization charge has been seen to cause a considerable shift in the band structure along the interface of a hybrid nanocomposite, as has been observed before. For the upward polarization state, the photovoltaic effect, and the modification of band structure at the $Au/[P(o\text{-}PDM + m\text{-}PDM)/ZrO_2]^{NC}$/p-Si interface are shown in Fig. 19, as is the mechanism of the photovoltaic effect. In this situation, a downward band bending with built-in field (E_{bi}) may be generated at the interface between the hybrid nanocomposite

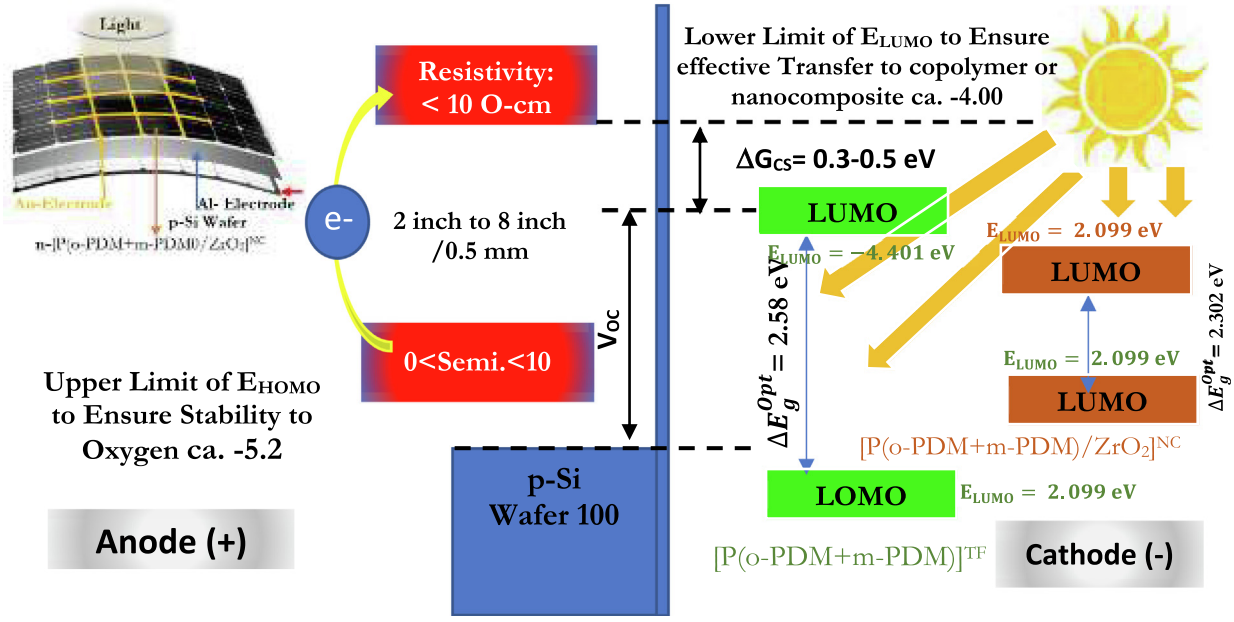

Fig. 19. Schematic of the energy band diagrams and Mechanism of photovoltaic response for the Au/[P(o-PDM + m-PDM)]^{TF} Or [P(o-PDM + m-PDM)/ZrO_2]^{NC} /p-Si/Al heterostructure and the corresponding insets show the signs and directions of V_{oc} and..I_{sc}

and the p-Si wafer, generating a positive photovoltage and a negative photocurrent, while a virtually flat band can develop at the interface between /[P(o-PDM + m-PDM)/ZrO_2]^{NC}/p-Si.

Conclusion

Oxidative polymerization with ferric chloride as an oxidizing agent has been proved to be a successful method to prepare ortho phenylene diamine and meta phenylene diamine copolymer. Addition of glycine and ZrO_2 nanoparticles to ortho phenylene diamine and meta phenylene diamine copolymer can improve thermal stability and optical properties. The bandgap energy was decreased from 2.29 and 1.98 eV due to the presence e of ZrO_2 nanoparticles. The interaction of [P(o-PDM + m-PDM)]^{TF} with [ZrO_2]^{NPs} improves charge transfer inside nanocomposite [P(o-PDM + m-PDM)]^{TF} thin films. The direct conductivity σ_{dc} of [P(o-PDM + m-PDM)]^{TF} and [P(o-PDM + m-PDM)/ZrO_2]^{NC} thin films are 37.79 × 10^{-5} and 49.75 × 10^{-5} S m^{-1}, respectively. The stability of the copolymer was proved by the extremely large negative value of HOMO, and the ability to supply electrons is indicated by the negative value of LUMO.

When two isolated molecules are attached (as polymerization case) by hydrogen bond and π bonding in phenylene diamine moiety, the lengths bond, centroid lengths, centroid angle and dihedral angle will decrease to half results from the interaction between Zr^{4+} and nitrogen atoms to form nanocomposite results from.

The prepared nanocomposite has a promising application in photovoltaic device. A heterojunction made of Au/[P(o-PDM + m-PDM)/ZrO_2]^{NC}/p-Si/Al had fill factors and power conversion efficiency of 56.72% and 9.07%, respectively, at 240 mW/cm^2.

Declaration of Competing Interest

The authors declare that they have no known competing financial interests or personal relationships that could have appeared to influence the work reported in this paper.

Acknowledgement

This research work was funded by Institutional Fund Projects under grant no. (IFPIP: 307 – 829 – 1442). Therefore, the authors gratefully acknowledge technical and financial support from the Ministry of Education and King Abdulaziz University, DSR, Jeddah, Saudi Arabia.

References

[1] L. Petti, N. Münzenrieder, C. Vogt, H. Faber, L. Büthe, G. Cantarella, et al., Appl. Phys. Rev. 3 (2016) 021303.
[2] N.M. Hosny, M.S. Zoromba, G. Samir, S. Alghool, J. Mol. Struct. 1122 (2016) 117–122.
[3] N.M. Hosny, N. Nowesser, A.S. Al-Hussaini, M.S. Zoromba, J. Mol. Struct. 1106 (2016) 479–484.
[4] M.S. Zoromba, N.A. El-Ghamaz, S. Alghool, J Inorg Organomet Polym Mater 25 (2015) 955–963.
[5] A. Noormohamadi, M. Homayoonfal, M.R. Mehrnia, F. Davar, Ceram. Int. 43 (2017) 17174–17185.
[6] A. Majedi, F. Davar, A. Abbasi, J. Env. Chem. Eng. 6 (2018) 701–709.
[7] F. Davar, A. Majedi, A. Mirzaei, Ceram. Int. 44 (2018) 19377–19382.
[8] X. Fang, Y. Xi, H. Jia, C. Chen, Y. Wang, Y. Song, et al., J. Ind. Eng. Chem. 88 (2020) 268–277.
[9] S. Cho, D. Kim, Y. Yun, J. Lee, T. Earmme, S.Y. Seo, et al., J. Ind. Eng. Chem. 92 (2020) 303–308.
[10] S. Khalili, H.M. Chenari, Thin Solid Films 741 (2022) 139031.
[11] H.M. Shinde, S.V. Kite, B.S. Shirke, K.M. Garadkar, J. Mater. Sci.: Mater. Electron. 32 (2021) 14235–14247.
[12] D. Kim, H. Li, M.H. Lee, K. Kim, S.N. Lim, J.Y. Woo, et al., J. Power Sources 484 (2021) 229254.
[13] T.A. Otitoju, P.U. Okoye, G. Chen, Y. Li, M.O. Okoye, S. Li, J. Ind. Eng. Chem. 85 (2020) 34–65.
[14] A. Ghosh, J. Clean. Prod. 276 (2020) 123343.
[15] M.H. Alaaeddin, S.M. Sapuan, M.Y.M. Zuhri, E.S. Zainudin, F.M. Al-Oqla, Renew. Sust. Energ. Rev. 102 (2019) 318–332.
[16] M.S. Zoromba, A.F. Al-Hossainy, M.H. Abdel-Aziz, Synth. Met. 231 (2017) 34–43.
[17] M.S. Zoromba, Spectrochim. Acta A Mol. Biomol. Spectrosc. 187 (2017) 61–67.
[18] M.S. Zoromba, M.H. Abdel-Aziz, Polymer 120 (2017) 20–29.
[19] M.S. Zoromba, M.H. Abdel-Aziz, M. Bassyouni, H. Bahaitham, A.F. Al-Hossainy, Journal Solid State, Electrochem. 22 (2018) 3673–3687.
[20] T. Salim, S. Sun, L.H. Wong, L. Xi, Y.L. Foo, Y.M. Lam, J. Phys. Chem. C 114 (2010) 9459–9468.
[21] D.W. Hatchett, M. Josowicz, Chem. Rev. 108 (2008) 746–769.
[22] S.V. Kite, A.N. Kadam, D.J. Sathe, S. Patil, S.S. Mali, C.K. Hong, et al., ACS Omega 6 (2021) 17071–17085.

[23] S. Samanta, P. Roy, P. Kar, Ionics 23 (2017) 937–947.
[24] U. Olgun, G. Mustafa, Gülfen, React., Funct. Polym. 77 (2014) 23–29.
[25] S. Samanta, R. Poulomi, K. Pradip, Polym. Adv. Technol. 28 (2017) 797–804.
[26] S. Sagar, N. Iqbal, A. Maqsood, M. Shahid, N.A. Shah, T. Jamil, et al., J. Compos. Mater. 49 (2015) 995–1006.
[27] R. da Rocha Rodrigues, R.L.C.G. da Silva, L. Caseli, L.O. Peres, Adv. Colloid Interface Sci. 285 (2020) 102277.
[28] K.H. Hwang, D.H. Kim, M.H. Choi, J.P. Han, D.K. Moon, J. Ind. Eng. Chem. 34 (2016) 66–75.
[29] A.F. Al-Hossainy, M.R. Eid, M.S. Zoromba, J. Electron. Mater. 48 (2019) 8107–8115.
[30] M. Abd El-Aal, R.T. Mogharbel, A. Ibrahim, N. Almutlaq, M.S. Zoromba, A.F. Al-Hossainy, et al., J. Mol. Struct. 1250 (2022) 131827.
[31] F. Davar, A. Hassankhani, M.R. Loghman-Estarki, Ceram. Int. 39 (2013) 2933–2941.
[32] A.F. Al-Hossainy, A.Y. Sediq, S.A. Mahmoud, Electron. Mater. Lett. 17 (2021) 188–206.
[33] M.H. Abdel-Aziz, E.S.Z. El-Ashtoukhy, M. Bassyouni, A.F. Al-Hossainy, E.M. Fawzy, S.M.S. Abdel-Hamid, et al., Carbon Lett. 31 (2021) 863–878.
[34] N. Almutlaq, A.F. Al-Hossainy, M. Sh Zoromba, J. Mol. Struct. 1227 (2021) 129712.
[35] X. Tu, Q. Xie, C. Xiang, Y. Zhang, S. Yao, J. Phys. Chem. B 109 (2005) 4053–4063.
[36] A.F. Al-Hossainy, J. Electron. Mater. 50 (2021) 3800–3813.
[37] S. Sahoo, J.-J. Shim, J. Ind. Eng. Chem. 54 (2017) 205–217.
[38] H. Mansour, E.M.F. Abd El Halium, N.F.H. Alrasheedi, M. Sh Zoromba, A.F. Al-Hossainy, J. Mater. Sci. Mater. Electron. 33 (2022) 5244–5264.
[39] A.K. Sarkar, P.K. Roy, Asian J. Res. Chem. 12 (2019) 241–247.
[40] N. Almutlaq, A.F. Al-Hossainy, Compos. Interfaces 28 (2021) 879–904.
[41] I.E. Wachs, C.A. Roberts, Chem. Soc. Rev. 39 (2010) 5002–5017.
[42] F. Ortéga, M.T. Pope, H.T. Evans, Inorg. Chem. 36 (1997) 2166–2169.
[43] Y. Du, J. Zhang, P. Peng, H. Su, S. Li, S. Pang, New J. Chem. 41 (2017).
[44] C. Calvo, R. Faggiani, Am. Mineral. 59 (1974) 1277–1285.
[45] A.S. Kalogirou, I.C. Christoforou, H.A. Ioannidou, M.J. Manos, P.A. Koutentis, RSC Adv. 4 (2014) 7735–7748.
[46] Z. Demircioğlu, C.C. Ersanli, S. Şaşmaz, J. Mol. Struct. 1181 (2019) 25–37.
[47] A.F. Al-Hossainy, M. Sh Zoromba, J. Mol. Struct. 1156 (2018) 83–90.
[48] A.F. Al-Hossainy, A. Ibrahim, Mater. Sci. Semicond. Process. 38 (2015) 13–23.
[49] S.A. Mahmoud, A.A. Al-Dumiri, A.F. Al-Hossainy, Vacuum 182 (2020) 109777.
[50] S. Tariq, M. Khalid, A. Raza, S.L. Rubab, S.F. de Alcântara Morais, M.U. Khan, et al., J. Mol. Struct. 1207 (2020) 127803.
[51] M. Miar, A. Shiroudi, K. Pourshamsian, A.R. Oliaey, F. Hatamjafari, J. Chem. Res. 45 (2021) 147–158.
[52] R. Srivastava, L. Sinha, M. Karabacak, O. Prasad, S.K. Pathak, A.M. Asiri, et al., Spectrochim. Acta A 136 (2015) 1205–1215.
[53] K. Zare, N. Shadmani, E. Pournamdari, J. Nanostructure Chem. 3 (2013) 1–6.
[54] B.H. Jeong, E.M.V. Hoek, Y. Yan, A. Subramani, X. Huang, G. Hurwitz, et al., J. Membrane Sci. 294 (2007) 1–7.
[55] A.F. Al-Hossainy, R.M. Abdelaal, W.N. El Sayed, J. Mol. Struct. 1224 (2021) 128989.
[56] M.J. Mayor-Lopez, J. Weber, Chem. Phys. Lett. 281 (1997) 226–232.
[57] S. Grimme, J. Antony, S. Ehrlich, H. Krieg, J. Chem. Phys. 132 (2010) 154104.
[58] Q. Li, Z. Li, Adv. Sci. 4 (2017) 1600484.
[59] G. Mohammed, A.M. El Sayed, W.M. Morsi, J. Phys. Chem. Solids 115 (2018) 238–247.
[60] A. Attar, R.D. Alharthy, M. Zwawi, M. Algarni, F. Albatati, M. Bassyouni, et al., J. Ind. Eng. Chem. 109 (2022) 230–244.
[61] I.H. El Azab, A.A. Gobouri, T.A. Altalhi, H.S. El-Sheshtawy, N. Almutlaq, H.A. Maddah, et al., Optik 247 (2021) 167971.
[62] S.M. Ibrahim, A. Bourezgui, A.F. Al-Hossainy, J. Polym. Res. 27 (2020) 1–18.
[63] N. Durante, A. Fortunelli, M. Broyer, M. Stener, J. Phys. Chem. C 115 (2011) 6277–6282.
[64] R. Srinet, S. Nandy, N.R. Patel, Ecol. Inform. 52 (2019) 94–102.
[65] S.M. Ibrahim, A.F. Al-Hossainy, Chem. Pap. 75 (2021) 297–309.
[66] N.M. Mahani, Medbiotech J. 5 (2021) 37–40.
[67] G.B. Sakr, I.S. Yahia, M. Fadel, S.S. Fouad, N. Romčević, J. Alloy. Compd. 507 (2010) 557–562.
[68] J.N. Hodgson, Optical absorption and dispersion in solids, Butler & Tanner Ltd., Lonodon, 2012.
[69] M.K. Priya, B.K. Revathi, V. Renuka, S. Sathya, P.S. Asirvatham, Mater. Today-Proc. 8 (2019) 37–46.
[70] M.S. Tolba, A.F. Al-Hossainy, A.M. Kamal, Eldean, O. Younis, Asian,, J. Org. Chem. 11 (2022) e202100801.
[71] B.M.M. Sudha, D. Kumar, Particul, Sci. Technol. 32 (2014) 624–631.
[72] H. Cui, Q. Li, S. Gao, J.K. Shang, J. Ind. Eng. Chem. 18 (2012) 1418–1427.
[73] S.A. Mahmoud, A.F. Al-Hossainy, E.R. Shaaban, Int. J. Energ. Res. 45 (2021) 20258–20269.
[74] S. Eymur, N. Tuğluoğlu, A. Apaydın, Ü. Akın, Ö.F. Yüksel, ECS J Solid State Sci Technol. 10 (2021) 051001.
[75] S.V. Kite, D.J. Sathe, S.S. Patil, P.N. Bhosale, K.M. Garadkar, Mater. Res. Express 6 (2018) 026411.